



ELSEVIER

Atmospheric Research 78 (2005) 103–145

ATMOSPHERIC  
RESEARCH

www.elsevier.com/locate/atmos

# Three-dimensional nonhydrostatic simulations of summer thunderstorms in the humid subtropics versus High Plains

Hsin-mu Lin, Pao K. Wang\*, Robert E. Schlesinger

*Department of Atmospheric and Oceanic Sciences, University of Wisconsin-Madison,  
1225 W. Dayton Street, Madison, WI 53706, USA*

Received 30 December 2003; received in revised form 30 November 2004; accepted 30 March 2005

---

## Abstract

This article presents a detailed comparison of cloud microphysical evolution among six warm-season thunderstorm simulations using a time-dependent three-dimensional model WISCDYMM. The six thunderstorms chosen for this study consist of three apiece from two contrasting climate zones, the US High Plains (one supercell and two multicells) and the humid subtropics (two in Florida, US and one in Taipei, Taiwan, all multicells). The primary goal of this study is to investigate the differences among thunderstorms in different climate regimes in terms of their microphysical structures and how differently these structures evolve in time. A subtropical case is used as an example to illustrate the general contents of a simulated storm, and two examples of the simulated storms, one humid subtropical and one northern High Plains case, are used to describe in detail the microphysical histories. The simulation results are compared with the available observational data, and the agreement between the two is shown to be at least fairly close overall.

The analysis, synthesis and implications of the simulation results are then presented. The microphysical histories of the six simulated storms in terms of the domain-integrated masses of all five hydrometeor classes (cloud water, cloud ice, rain, snow, graupel/hail), along with the individual sources (and sinks) of the three precipitating hydrometeor classes (rain, snow, graupel/hail) are analyzed in detail. These analyses encompass both the absolute magnitudes and their percentage contributions to the totals, for the condensate mass and their precipitation production (and depletion) rates, respectively.

---

\* Corresponding author. Tel.: +1 608 263 6479; fax: +1 608 262 7482.

*E-mail address:* pao@windy.aos.wisc.edu (P.K. Wang).

Comparisons between the hydrometeor mass partitionings for the High Plains versus subtropical thunderstorms show that, in a time-averaged sense, ice hydrometeors (cloud ice, snow, graupel/hail) account for ~70–80% of the total hydrometeor mass for the High Plains storms but only ~50% for the subtropical storms, after the systems have reached quasi-steady mature states. This demonstrates that ice processes are highly important even in thunderstorms occurring in warm climatic regimes.

The dominant rain sources are two of the graupel/hail sinks, shedding and melting, in both High Plains and subtropical storms, while the main rain sinks are accretion by hail and evaporation. The dominant graupel/hail sources are accretion of rain, snow and cloud water, while its main sinks are shedding and melting. The dominant snow sources are the Bergeron-Findeisen process and accretion of cloud water, while the main sinks are accretion by graupel/hail and sublimation. However, the rankings of the leading production and depletion mechanisms differ somewhat in different storm cases, especially for graupel/hail.

The model results indicate that the same hydrometeor types in the different climates have their favored microphysical sources and sinks. These findings not only prove that thunderstorm structure depends on local dynamic and thermodynamic atmospheric conditions that are generally climate-dependent, but also provide information about the partitioning of hydrometeors in the storms. Such information is potentially useful for convective parameterization in large-scale models.

© 2005 Elsevier B.V. All rights reserved.

*Keywords:* Thunderstorm simulations; Hydrometeor partitioning; Microphysical structure; Subtropical thunderstorms; High Plains thunderstorms; Nonhydrostatic cloud models

---

## 1. Introduction

Clouds and precipitation are paramount meteorological processes in the general public's concept of "weather". Deep precipitating convective cloud systems in the form of thunderstorms, in particular, have long posed especially acute concern to society because of their attendant risks of injuries, deaths and damage to property and crops from lightning, floods, hail, strong straight-line winds, tornadoes or a combination among these phenomena (e.g., [Kessler and White, 1981](#)). Over the last 10–15 years, the societal impacts of convective storms have become more urgent amid mounting circumstantial signs of climate change qualitatively consistent with decadal-scale climate predictions using general circulation models (GCMs), designed to gauge the effects of doubling the concentration of atmospheric carbon dioxide ([Price and Rind, 1994](#); [Gregory and Mitchell, 1995](#); [Frei et al., 1998](#)). These effects, projected to the end of the 21st century, globally and annually averaged, include the following: warming of several Celsius degrees from the earth's surface through the midtroposphere, increased atmospheric water vapor content roughly sufficient to maintain the relative humidity at most levels, more frequent exceptionally heavy 1-day rainfalls, and more frequent thunderstorms as inferred from higher parameterized counts of lightning flashes. While great care must be taken when attempting to link global warming and an upward trend in the atmospheric CO<sub>2</sub> concentration ([Michaels and Stooksbury, 1992](#)), data from Mauna Loa Observatory during 1958–2002 do show an increase of ~18% in the mean annual (deseasonalized) CO<sub>2</sub> concentration in a systematic and accelerating trend ([Keeling and Whorf, 2003](#)).

Griffiths et al. (1993) have suggested three possible uses of GCMs to evaluate the impact of climate change on severe thunderstorm climatology in a region, based on comparing the results of simulations with and without including the climate change in the input: (a) look for suitably large correlations, if any, between model-based circulation indices and storm climatology parameters, in order to use the former as proxies for the latter; (b) note the frequency of vertical atmospheric profiles favorable to severe storms; or (c) note the frequency of sea-level synoptic patterns favorable to severe storms.

However, GCMs pose major obstacles to inferring the impact of climate change on severe storm climatology in the ways Griffiths et al. (1993) suggest. Method (a) cannot ensure suitably strong correlations, while methods (b) and (c) require a much finer horizontal grid mesh than the few hundred kilometers typical of GCMs. Also, being tens of times wider than the active convective cores responsible for severe weather, GCM grid cells can explicitly resolve only stratiform cloud decks such as those spawned by aging convective systems. Thus, convection must be parameterized in GCMs, posing an inherently formidable challenge because the microphysical processes within the convective cells feed back crucially to the cloud scale and mesoscale before eventually influencing the GCM-resolvable scales (Grabowski, 2000). Yet most convective parameterizations in the more widely used GCMs treat microphysics very crudely, typically adapting the now-classic algorithms of Manabe et al. (1965), Kuo (1974) or Arakawa and Schubert (1974), as noted by Emanuel and ivkoviaë-Rothman (1999), although a few more recent GCMs have made some headway with more sophisticated microphysical parameterizations in the forcing of grid-resolvable moisture fields (e.g., Fowler et al., 1996; Fowler and Randall, 1996a,b). But even with improved convective parameterizations, the coarseness of the horizontal grids in GCMs would preclude proper handling of microphysical feedback because it is communicated upscale much faster than in nature (Grabowski, 2000).

The need to better represent convective cloud properties in GCMs motivated this study. We feel that the current convective cloud parameterizations used in GCMs can be improved by including the effect of different geographic zones on the microphysical structure of convective clouds. Conceivably, clouds in different geographical locations (for example, middle versus low latitudes, over ocean versus over land) may have different microphysical structure. One obvious example is the hydrometeor partitioning, e.g., the amount of ice versus liquid mass and the vertical extent of ice versus liquid layers. These structural differences would be computed directly if the GCMs were able to solve the microphysical equations governing the hydrometeor growth, but this is obviously not the case. There is also no extensive observational database of convective clouds that can supply this information. One approach that can potentially do so is to perform cloud model simulations for a wide range of convective clouds in various locations all over the world. This approach would be meaningful if (1) the model results agree reasonably well with available observations, and (2) the results show that the microphysical structure of a specific kind of mature convective cloud is quasi-steady state so that the modeled hydrometeor partition is reasonably representative.

The present study was performed to investigate the feasibility of the approach as suggested above. We limited our attention to two geographical locations, namely the

midlatitude US High Plains and humid subtropics. The model results provide information not only on the dynamics and thermodynamics but also on details of the microphysical processes.

The findings, even though limited to two climatic regions, suggest that it is meaningful to use output from thunderstorm simulations to determine time-averaged quasi-steady hydrometeor partitionings, and hence the approach suggested previously turned out to be feasible.

Such findings are potentially useful for other types of studies as well. For example, [Flossmann et al. \(1985, 1987\)](#), [Flossmann and Pruppacher \(1988\)](#) and [Flossmann \(1998\)](#) used a cloud model to study the wet removal of aerosol particles and trace gases in the atmosphere and demonstrated that cloud microphysics have significant impacts on the cleansing ability of cloud and precipitation system. The understanding gained from the present study will certainly be beneficial to the research of wet removals of atmospheric chemicals in different climatic regimes.

The details of our findings are reported here. First, we will describe briefly the cloud model used for the present study. Next, the brief observed histories of all six storms simulated will be described, followed by examples of the simulated storms and their comparison with observations, such as the wind and hydrometeor fields. Finally, the comparison of midlatitude versus subtropical storm microstructures based on simulated results, and a summary of our findings, will be given.

## **2. Brief description of WISCDYMM**

The cloud model used in this study is WISCDYMM (the Wisconsin Dynamic and Microphysical Model), originated by [Straka \(1989\)](#) and subsequently modified by middle author Wang's research group ([Johnson et al., 1993, 1994](#); [Lin and Wang, 1997](#); [Lin, 2000](#); [Wang, 2003, 2004](#)). It is a three-dimensional, nonhydrostatic, primitive equation, quasi-compressible cloud model. The time step size, assumed uniform, is dictated by quasi-compressible computational stability requirements. For the present study, the grid mesh is 1.0 km horizontally and 0.5 km vertically, with corresponding dimensions of 55 and 20 km for the model domain, while the time step is 3 s. A sensitivity test of vertical resolution has been done by running two cases at 0.2 km and the results are very similar to the present results.

WISCDYMM features a bulk microphysics parameterization that entails water vapor and five hydrometeor types: cloud water, cloud ice, rain, graupel/hail and snow, with 37 individual transfer rates (source/sink terms) adapted largely from [Lin et al. \(1983\)](#) and [Cotton et al. \(1982, 1986\)](#).

The lateral boundary conditions are similar to those in [Klemp and Wilhelmson \(1978\)](#). Both the upper and lower boundaries are rigid lids. Variables at the top are held undisturbed, while reflection of upward-propagating gravity waves off the lid is suppressed as in [Clark \(1977\)](#) by imposing an upper-level Rayleigh damping layer that abuts it. The lower boundary has four options: free-slip with no surface heat flux; semi-slip with no surface energy budget; no-slip with heat flux and no surface energy budget; or no-slip with heat flux, insolation and surface energy budget.

Convection in the model is initiated by a technique similar to that used by Klemp and Wilhelmson (1978) and Straka (1989). A warm thermal bubble 20 km wide and 4 km deep is centered 2 km above ground level (AGL) in a horizontally homogeneous environment. The maximum thermal perturbation is 3.5 K in the center of the bubble, and the mixing ratio is adjusted to keep the relative humidity (RH) the same as that in the undisturbed sounding. All six cases are initialized by the same thermal bubble.

The current version of WISCDYMM uses forward time differencing and sixth-order flux-conservative Crowley spatial differencing (Tremback et al., 1987). To suppress nonlinear instability, a fourth-order numerical diffusion operator with a constant coefficient, as in Klemp and Wilhelmson (1978), is added in the discretized predictive equations at each time step.

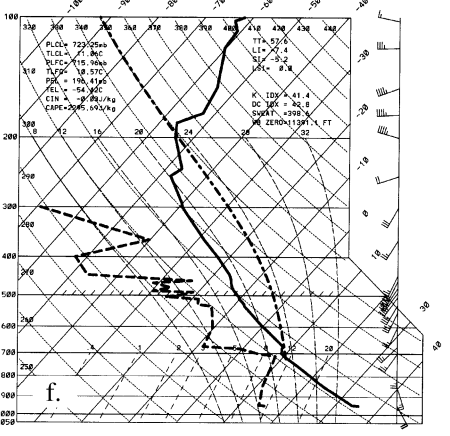
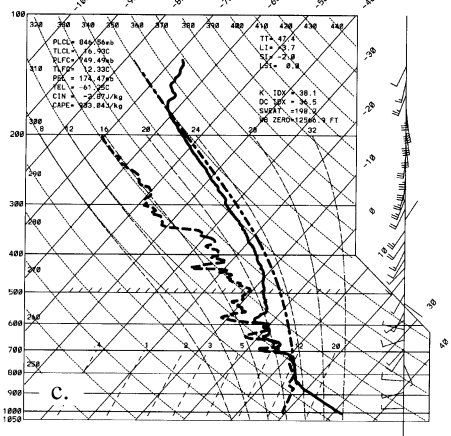
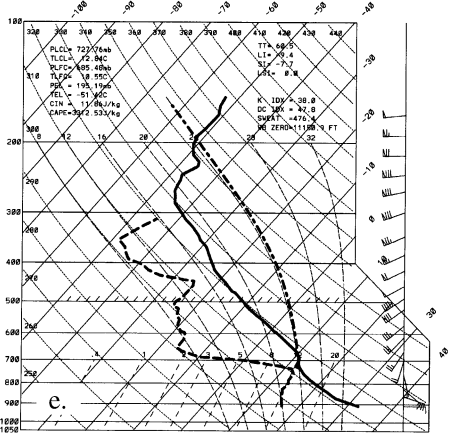
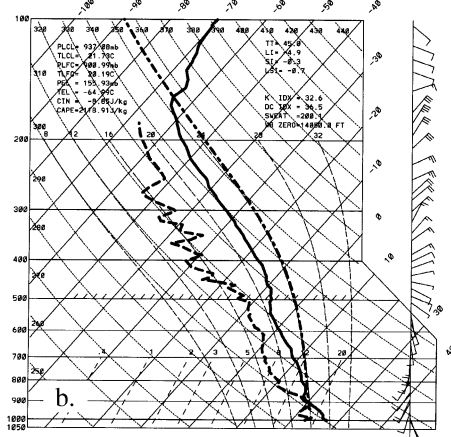
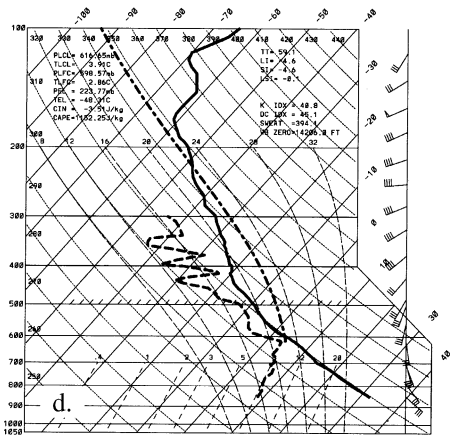
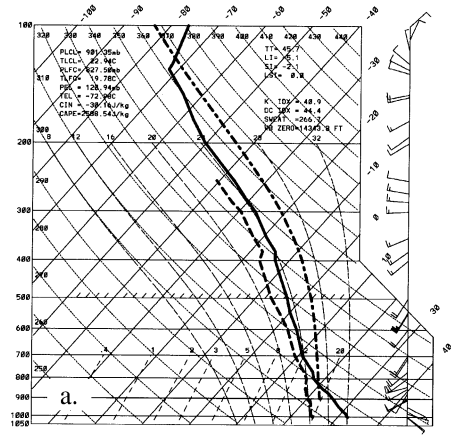
The original WISCDYMM has two versions: one using bulk parameterization to treat hail production, the other uses a bin-techniques to study the hail growth in greater detail. The present study used the former and we do not determine the hail size distribution here.

### 3. The storms chosen for the present study

Three cases apiece, in the humid subtropics and US High Plains, are simulated in this study, involving one severe storm and two moderate ones in each region. This layout enables us to compare the storms' characteristics in the same region as well as in the different regions. The simulated subtropical storms are (a) 15 August 1991 Convection and Precipitation/Electrification Project (CaPE) case (Yuter and Houze, 1995a,b), (b) 29 July

Table 1  
Characteristics and indices of the observed soundings in the subtropics and High Plains

	Subtropics			High Plains			
	Taipei 6/21/1991	CaPE 7/29/1991	CaPE 8/15/1991	CCOPE 8/02/1981	NHRE 6/12/1976	NDTP 6/29/1989	
Sub-cloud mixing ratio (average) g/kg	20	17.5	14	12	8	10	
Surface	$P_{mb}$	1001.3	1000	1005.4	909.7	850	949.5
	$T_{\circ C}$	32.1	27.3	31.9	32.9	31.85	35.0
LCL	$P_{mb}$	911.53	937.08	846.56	727.76	616.65	723.25
	$T_{\circ C}$	23.9	21.7	16.9	12.8	3.9	11.1
LFC	$P_{mb}$	867.08	900.99	749.49	685.48	598.57	715.96
	$T_{\circ C}$	22.0	20.2	12.3	10.6	2.86	10.6
EL	$P_{mb}$	115.84	155.93	174.47	195.19	223.77	196.41
	$T_{\circ C}$	-73.7	-65.0	-61.3	-51.4	-48.3	-54.4
CAPE <sub>j/kg</sub>		3335.80	2118.91	933.04	3312.53	1152.25	2295.69
CIN <sub>j/kg</sub>		-22.76	-8.85	-2.87	11.86	-3.51	-0.03
Total totals index		42.7	45.0	47.4	60.5	59.1	57.6
Lift index		-6.0	-4.9	-3.7	-9.4	-4.6	-7.4
Showalter index		0.9	-0.3	-2.0	-7.7	-4.6	-5.2
K index		37.9	32.6	38.1	38	40.8	41.4
Deep convective index		42.3	36.5	36.5	47.8	45.1	42.8
Severe weather threat index		266.7	200.1	198.2	476.4	394.1	398.6
Wet bulb zero <sub>m</sub> (AGL)		4361.0	4277.5	3822.4	2445.4	3010.9	2968.4



1991 CaPE case (Ramachandran et al., 1996), and (c) 21 June 1991 Taipei case (Jou, 1994; Lin and Wang, 1997). The simulated High Plains storms are (a) 2 August 1981 Cooperative Convective Precipitation Experiment (CCOPE) case (Wade, 1982; Miller et al., 1988; Musil et al., 1986; Johnson et al., 1994), (b) 22 June 1976 National Hail Research Experiment (NHRE) case (Fankhauser, 1982; Foote, 1984; Straka, 1989), and (c) 28 June 1989 North Dakota Thunderstorm Project (NDTP) case (Orville et al., 1990; Klimowski, 1994). It has been proven that WISCDYMM simulates High Plains thunderstorms realistically as shown by the simulation of the 2 August 1981 CCOPE case (Johnson et al., 1993, 1994) and the 22 June 1976 NHRE case (Straka, 1989). The model results provide information not only on the dynamics and thermodynamics but also on details of the microphysical processes. Although the microphysical parameterizations of WISCDYMM are based on observations in midlatitudes, the question of whether we can use this model in subtropical areas has been answered affirmatively by a previous analysis of the 21 June 1991 Taipei simulation (Lin and Wang, 1997). The overall results of that study seem to agree well with the observations and offer evidence that WISCDYMM can simulate usefully the storms in subtropical areas as well as the High Plains.

The characteristics of the soundings in our study, including convective indices, are shown in Table 1. The importance of these characteristics and indices alone will be discussed in a later section. Table 1 clearly shows that the High Plains cases possess a lower wet-bulb zero height than the cases in the subtropics, indicating that the High Plains environments have high potential to produce hail, including at the ground. Heavy rain occurred instead at the ground in the subtropical cases, due to the smaller depth in which to form hail and a greater probability of its melting in the significantly thicker warm cloud layer before reaching the ground.

Figs. 1 and 2 show, respectively, the Skew  $T$ -log  $P$  soundings and environmental wind hodograph from soundings used as the initial conditions for the simulations of the six chosen storms. For details of the observed characteristics and history of the chosen storms, the readers are referred to the respective papers cited in the beginning of this section. All six storms studied here had been observed by rather extensive ground-based networks, which provide adequate data for comparison with model results. We will use one subtropical case as an example to illustrate the general features of the cloud model results. Two examples of the simulation results will be presented in detail and compared with the observations.

#### 4. An example of the simulated storms

In this section, we will use the CaPE, 29 July 1991 case to illustrate the simulated cloud microphysical features and to compare with observations. The analysis and comparison will include kinematics, thermodynamics, radar reflectivity structure, and precipitation patterns.

---

Fig. 1. Skew  $T$ -log  $P$  soundings at (a) Panchiao, Taiwan at 1200 LST on 21 June 1991; (b) Cape Canaveral Air Force Station, FL at 2030 UTC on 29 July 1991; (c) Deer Park, FL at 1830 UTC on 15 August 1991; (d) Potter, NE at 1450 MDT on 22 June 1976; (e) Knowlton, MT at 1746 MDT on 2 August 1981; (f) Bismarck, ND at 0000 UTC on 29 June 1991. The heavy dash-dot line represents undiluted parcel ascent from the surface to the LCL then follows the moist adiabatic condition. The heavy solid and dash line represents temperature and humidity respectively. Wind vectors shown on the right border are represented as hodograph in Fig. 3.

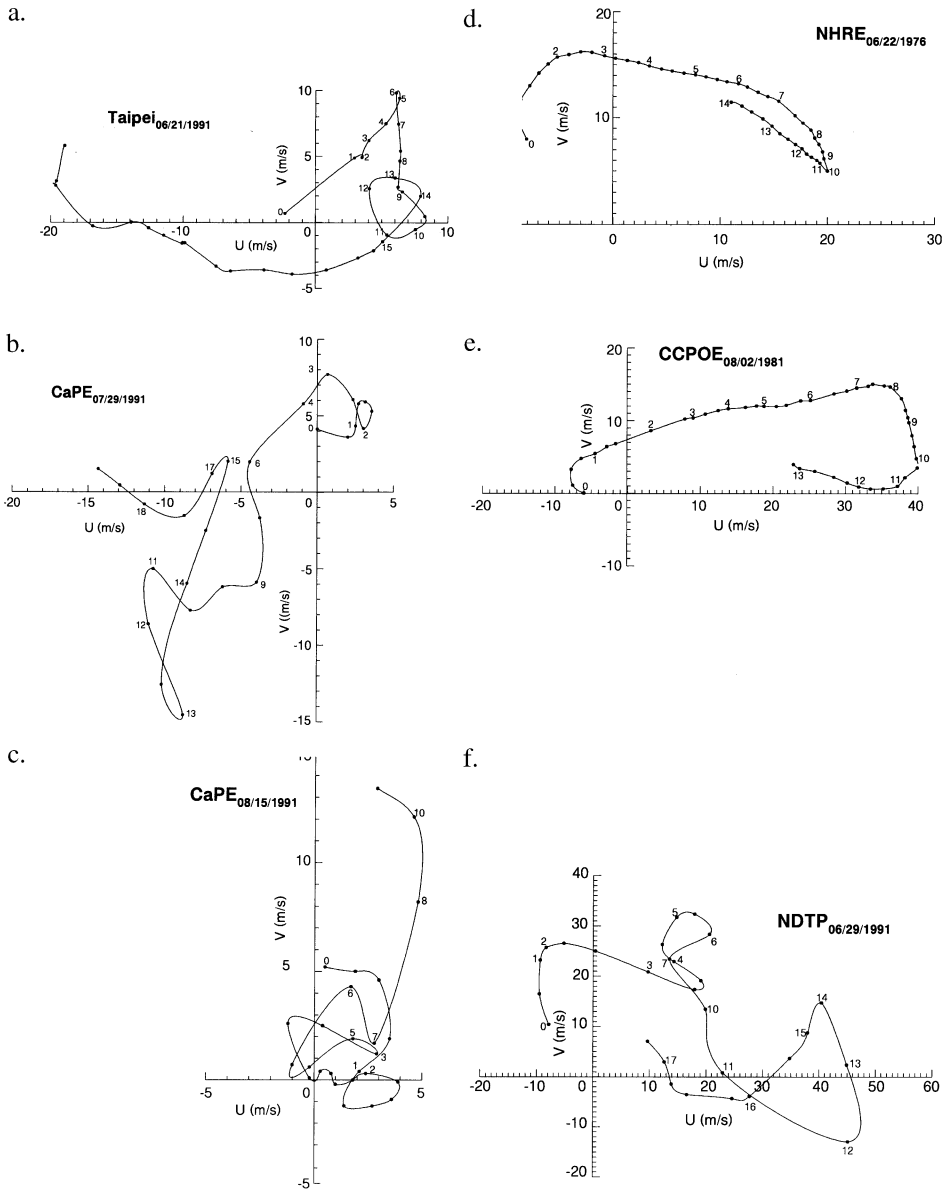


Fig. 2. Environmental wind hodograph from soundings at (a) Panchiao, Taiwan at 0000 UTC (0800 LST) on 21 June 1991; (b) Cape Canaveral Air Force Station, FL at 2030 UTC on 29 July 1991; (c) Deer Park, FL at 1830 UTC on 15 August 1991; (d) Potter, NE at 1450 MDT on 22 June 1976; (e) Knowlton, MT at 1746 MDT on 2 August 1981; (f) Bismarck, ND at 0000 UTC on 29 June 1991. The marked numbers represent height AGL (km).

Exclusive of the early updraft peak of  $56 \text{ m s}^{-1}$  from the initial perturbation, a strong updraft with maximum velocities about  $30 \text{ m s}^{-1}$  develops after spin-up time by 90 min in this simulation (Fig. 3). That value is similar to the  $25 \text{ m s}^{-1}$  detected by the T-28 aircraft (Ramachandran et al., 1996). Time evolution of the vertical cross-sections for the hydrometeor fields in the updraft core from 70 to 120 min is shown in Fig. 4 for the  $X$ - $Z$  slab and Fig. 5 for the  $Y$ - $Z$  slab. This period encompasses the quasi-steady and mature stages of the simulated storm life cycle.

#### 4.1. Cloud water

The maximum cloud water mixing ratio descends from  $\sim 7$  to 3 km by 90 min and goes back to  $\sim 6$  km thereafter. The temperature in this migrating core is between  $6^\circ\text{C}$  and  $-15^\circ\text{C}$ . Cloud base is as low as 0.6 km, approximately the same level as observed. Cloud water exists as high as 10 km, at temperatures near  $-38^\circ\text{C}$ . There is rapid depletion of liquid water near 10 km, approximately the level of the maximum updrafts.

#### 4.2. Cloud ice

Cloud ice is located generally above 8 km in the updraft core, at temperatures below  $-20^\circ\text{C}$ . The largest mixing ratios are located at and just above the updraft maximum, and mainly overlap the cloud water volume. The core of the cloud ice is at  $\sim 10$ – $11$  km and  $-38^\circ\text{C}$  to  $-43^\circ\text{C}$ . Cloud ice grows in these regions mainly by vapor deposition. The cloud ice mixing ratio and its areal coverage parallel the extent and strength of the updraft (Figs. 4 and 5). In the upper levels of the storm, advection of ice crystals by strong northeasterly winds increases the relative humidities south and west of the updraft, resulting in an expanding anvil from 90 to 120 min. Strong divergence at the tropopause also spreads the anvil south and north.

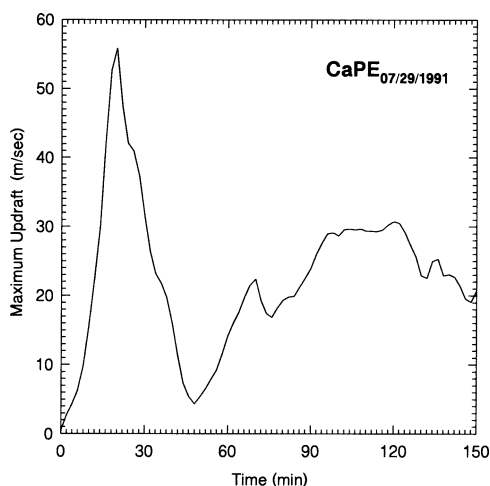
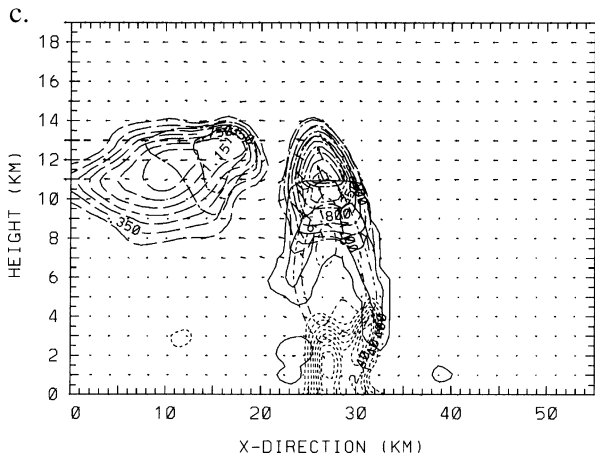
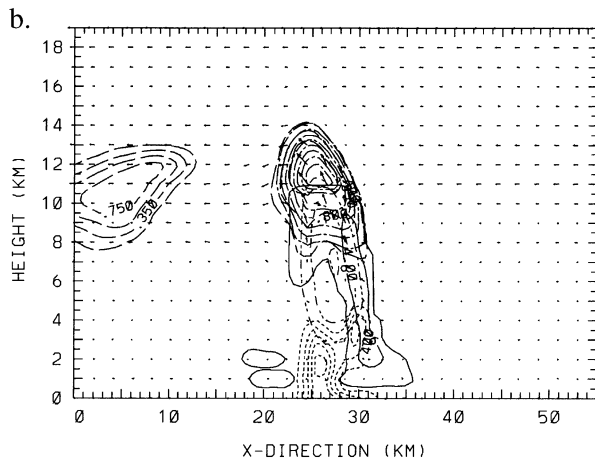
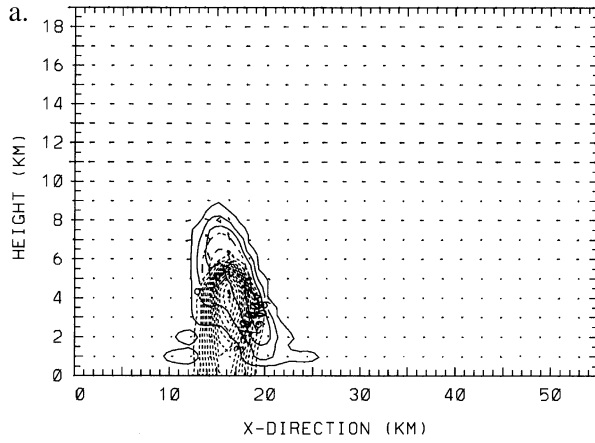


Fig. 3. Time evolution of the maximum updraft velocity in the simulated storm for CaPE, 29 July 1991.



### 4.3. Rain

Rain exists primarily below the melting level (4.5 km), except in the updraft core where freezing levels are as much as 0.5 km higher than ambient. Most rain falls below the updraft core in a small downdraft core and in the updraft below the hail and cloud water volumes. Maximum surface mixing ratios average approximately  $4.5 \text{ g kg}^{-1}$  during 70–120 min (Fig. 6), showing the propagation of rainfall and the development of successive individual convective elements. As the storm enters a quasi-steady state, the rain core is located between 1.5 and 4 km, primarily in the downdraft and secondarily in the updraft, evaporating and regenerating in these respective regions.

### 4.4. Snow

Snow is the most widely spreading precipitating hydrometeor in the simulation, with significant mixing ratios as far as 30 km south of the main storm shaft by 120 min (Fig. 5). Nearly all of the snow is above the  $-13 \text{ }^{\circ}\text{C}$  level (7.0 km), while the top of the snow layer rises from 12.0 km at 70 min to 15 km at 120 min. The snow volume is shallower than it is wide. After 80 min, as the storm assumes a quasi-steady state, the anvil begins to expand southward due to upper-level divergence from the updraft, coupled with relatively strong northerly winds. In the updraft shaft, the snow base is generally suspended aloft. Weaker updraft outside of the main storm shaft, with northerly upper-level flow and southerly midlevel flow (Fig. 5), recirculates some of the snow precipitated from the anvil. This mechanism maintains the growth of ice in the upper portion of the storm. The first snow crystals, shortly after the initial production of cloud ice crystals, occur only 6 min into the simulation via the Bergeron-Findeisen process.

Snow is important to the production and growth of small hail/graupel and cloud ice particles, especially below 8 km ( $-20 \text{ }^{\circ}\text{C}$ ), where snow rimes significantly due to high cloud water content.

### 4.5. Hail/graupel

In the simulation, considerable small hail/graupel appears by 12 min, after which the early updraft decreases in response to precipitation loading (Fig. 3) around 20 min when graupel/hail falls from upper levels. Most of the hail melts and sheds short of the ground, with maximum concentrations around 5.5 km ( $-6 \text{ }^{\circ}\text{C}$ ). The shaft of heaviest hail extends nearly vertically within the updraft core from upper levels into the midlevels. The maximum mixing ratio increases from  $4.3 \text{ g kg}^{-1}$  at 70 min to  $8.0 \text{ g kg}^{-1}$  at 90 min, and

---

Fig. 4. Simulated hydrometeor mixing ratios and storm-relative vector wind projection field for the CaPE storm of 29 July 1991, in  $X$ - $Z$  (east–west) vertical cross-sections through the maximum updraft as of (a) 80 min, (b) 100 min, (c) 120 min. Solid, short dashed, dash-dot, long dashed and dash-dot-dot lines represent mixing ratio contours of cloud water, rain, cloud ice, snow and graupel/hail, respectively. Minimum contour values for cloud water, rain, cloud ice, snow, and hail/graupel are 0.05, 0.4, 0.2, 0.15 and  $2.0 \text{ g kg}^{-1}$ , respectively. The increments for cloud water, rain, cloud ice, snow, and hail/graupel are 0.5, 0.5, 0.2, 0.2 and  $2.0 \text{ g kg}^{-1}$ , respectively.

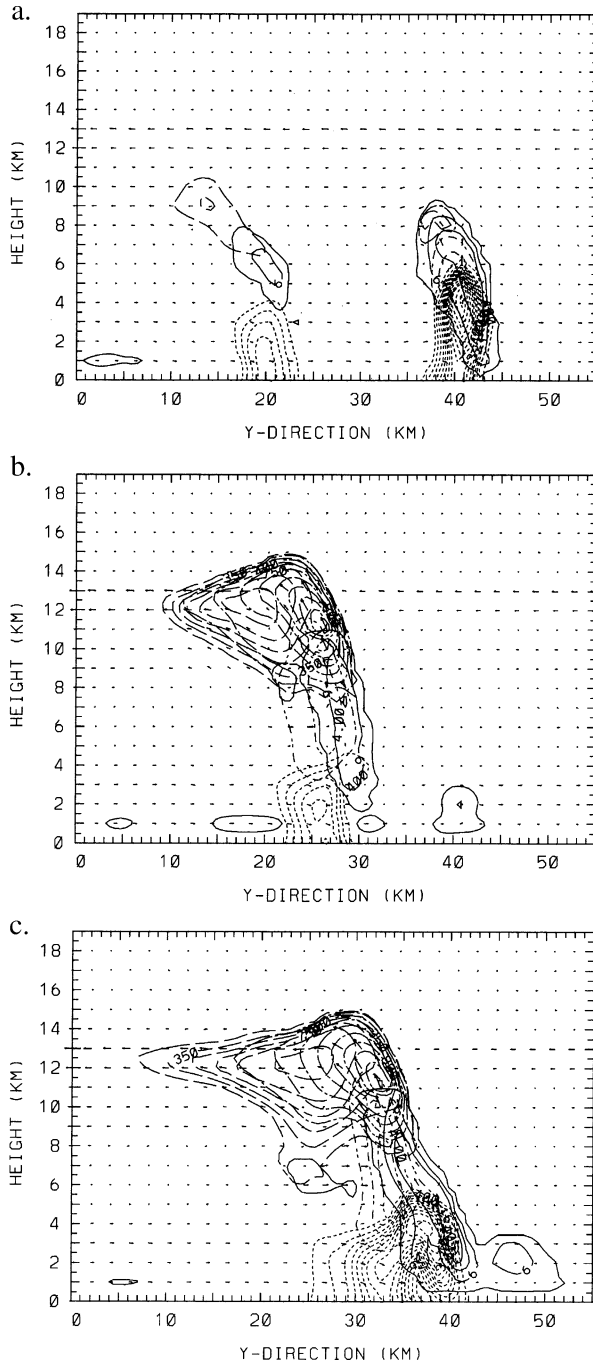


Fig. 5. Same as Fig. 4 except for Y-Z (south-north) vertical cross-sections.

then decreases to  $6.5 \text{ g kg}^{-1}$  at 120 min. Most of the hail below 2 km has melted into rain. Other hail particles further aloft are vented to the upper levels and into the anvil, undergoing little further growth.

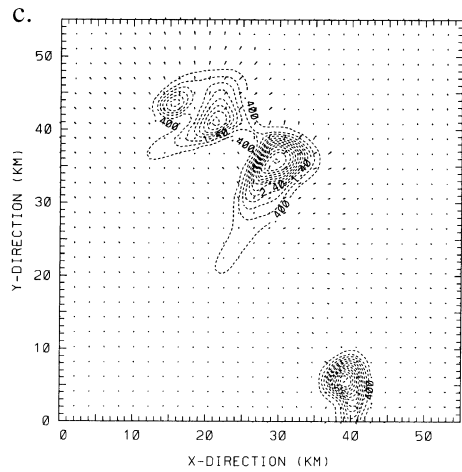
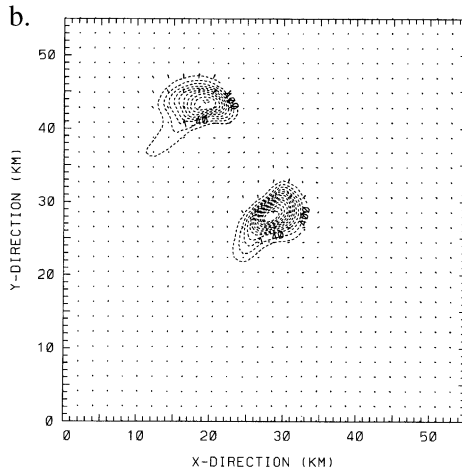
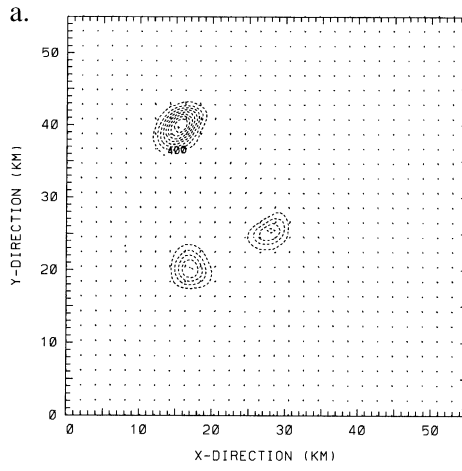
#### 4.6. Discussion and comparison with observations

In this mature multicellular storm, extending well above 14 km, rain is present from the ground to about 6 km. Cloud ice, snow and graupel/hail extend from about 4–15 km above surface. At high altitudes, where most of the snow and cloud ice grow, the ice-phase hydrometeors extend mainly downstream. Supercooled rain extends well above the freezing level of 4.5 km, overlapping the main low-level hail zone. Hail exists well below 4.5 km, and mainly passes through the rain region where downdrafts dominate (Figs. 4 and 5), and near the interface between the updraft and downdraft, in fairly good agreement with the T-28 aircraft observations which show the predominant hydrometeor type at the interface to be small to medium-size graupel (Ramachandran et al., 1996). In addition to the low-level downdrafts, Figs. 4 and 5 show significant upper-level downdrafts (~8–12 km) of  $\sim -5 \text{ m s}^{-1}$  next to the main updraft. This convective system is imbedded in quite weak vertical shear, and the rain region is right under the region of graupel/hail, whose core is down near the  $0^\circ\text{C}$  level with modest separation from the rain core, again suggesting that the rain comes mainly from melting and shedding of graupel/hail. Again, wet growth appears important to the production and depletion of rain and hail, as will be elaborated later.

The simulated midlevel radar echoes shown in Fig. 7 illustrate the development of the individual cells. Each cell evolves similarly. These storms have a southwest–northeast orientation with maximum reflectivities of more than 60 dBZ. These maxima and the successive storm development in the lower part of each plot (Fig. 7) are similar to the Cells B and C in “Storm 2” as observed from T-28 aircraft (Ramachandran et al., 1996).

During the simulation, the ice hydrometeors are mainly 4–14 km AGL as shown in previous figures. The observed developing “Cell C” is resembled in Fig. 7c. The simulation shows that the large reflectivities at 5.25 km ( $-6^\circ\text{C}$ ) come from the mixture of hail and supercooled rain to the south, supercooled rain and high cloud water concentrations to the north. The PMS 2D-P images obtained during the T-28 penetration at the  $-6^\circ\text{C}$  level show a mixture of spherical graupel and raindrops within cell B, then exclusively graupel in the region between Cells B and C. The central portions of Cell C showed high cloud water concentrations and supercooled rain (Ramachandran et al., 1996), fairly well simulated by our model.

We have made similar analyses and comparison with observation for the remaining five storm cases. Comparisons between the simulated and observed radar echo patterns have indicated that the locations and magnitudes of maximum radar reflectivity agree well with the observations. In one case (Taipei, 21 June 1991), for which our comparisons included simulated versus observed surface rainfall, the agreement was good in that respect as well. While we understand that the model has its limitations due to many factors (parameterizations, initial conditions, numerics, etc.), we feel that the structures and developmental histories of the simulated storms are sufficiently close to those of the real storms for the model results to be used as substitutes for them in studying the general microphysical histories of the storms in the two contrasting climatic regimes. Detailed bulk



microphysical analyses and synthesis of model results will be presented in the following section using two examples.

## 5. Two examples of microphysical structures of warm season thunderstorms in two different climate regimes

Detailed microphysical aspects of two simulated storms, one subtropical and one High Plains, in our study will be examined as examples for each climate regime. The overall microphysical structures of warm season thunderstorms in the two different climate regimes will be summarized in the balance of this paper.

### 5.1. Subtropical case: CaPE, 29 July 1991

On the basis of the information shown in Table 1, particularly the vertically averaged mixing ratios in the subcloud layer, the maritime subtropical cases have more abundant water vapor sources than the High Plains ones despite similar surface temperatures, resulting in lower and warmer cloud bases. This suggests that warm microphysical processes are the major hydrometeor sources early in the subtropical thunderstorm evolution, with cold microphysical processes dominating thereafter. We choose the simulated 29 July 1991 CaPE storm to illustrate the subtropical case.

The updraft (Fig. 3) decreases rapidly around 20 min in response to precipitation loading and descent of hail/graupel from the upper levels. Rain mass increases due to shedding and melting of hail/graupel but then decreases as the initial storm dissipates. Because the updraft weakens, the heavier hydrometeors (hail/graupel, large raindrops) cannot remain suspended aloft and fall to the ground while the lighter hydrometeors (cloud ice, snow, cloud water) remain in the upper levels and exert little influence. Fig. 8 shows that for hydrometeors other than cloud water, total mass grows initially but then decreases when the initial storm begins to dissipate and a new one begins to develop. At the end of the initial storm (~40–50 min), the percentages (Fig. 9) of snow and cloud water increase rapidly while the other percentages decrease as evidence of the initial cell's dissipation.

With domain-integrated mass partitioning of 26% apiece for cloud water and rain, 34% snow, 12% hail/graupel and 2% cloud ice, the dissipating initial cell and its newly developed successor coexist at 52 min. The new cell develops at the expense of the water sources supporting the initial storm. Beginning at 56 min when the new system takes precedence (Fig. 8), hail/graupel, rain and cloud ice masses grow steadily, and their percentages stabilize at ~66 min (Fig. 9). After that, rain and hail/graupel increase rapidly in mass to 2900 and 2500 KT, respectively, at 120 min. After 56 min, the liquid water phase dominates, and peaks before the ice phase does (Fig. 9). This indicates that warm microphysics in the lower cloud region precedes the onset of the cold microphysical processes in the upper cloud region. The details of these phenomena are clarified in the following analysis of individual microphysical processes.

---

Fig. 6. Simulated rain water mixing ratio and storm-relative horizontal wind projection field for the CaPE storm of 29 July 1991 on the surface ( $Z=0$ ) as of (a) 80 min, (b) 100 min, (c) 120 min. Minimum contour and contour interval are 0.4 and 0.5  $\text{g kg}^{-1}$ , respectively.

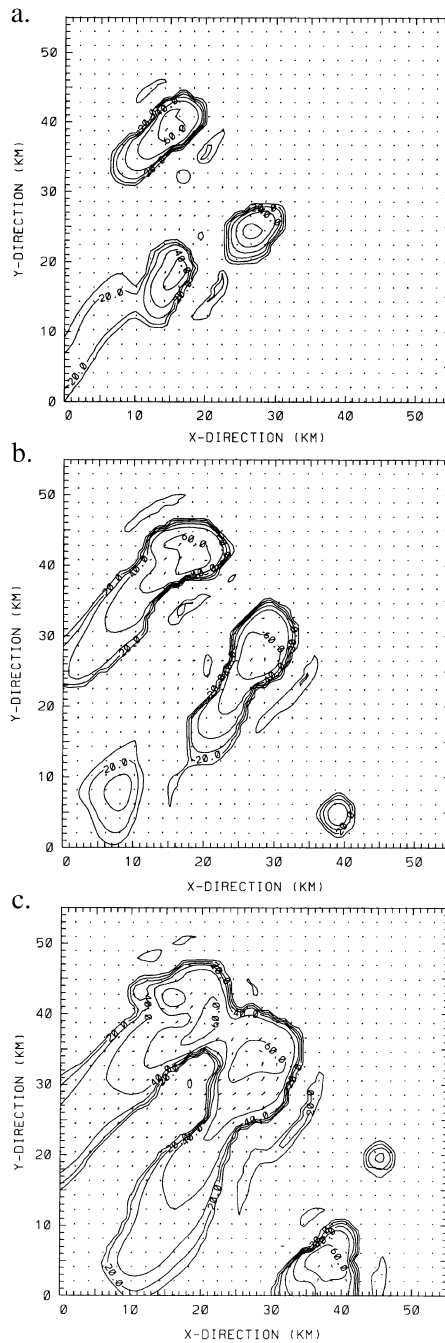


Fig. 7. Simulated radar reflectivity and storm-relative horizontal wind projection field for the CaPE storm of 29 July 1991 at  $Z=5.25$  km as of (a) 80 min, (b) 100 min, (c) 120 min. Minimum contour and contour interval are 10 and 10 dBZ, respectively.

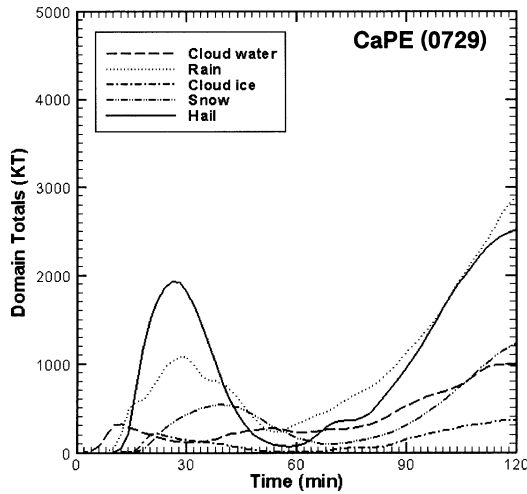


Fig. 8. Time evolution of simulated total condensate mass, integrated over the entire simulation domain ( $55 \times 55 \times 20 \text{ km}^3$ ), for both non-precipitating hydrometeors (cloud water and cloud ice) and precipitating ones (rain, snow and graupel/hail) in the simulated storms for the subtropical case of CaPE, 29 July 1991.

The steady growth of each hydrometeor mass after 60 min, especially for rain and hail/graupel (Fig. 8), again indicates widening precipitation areas rather than increasing precipitation rates. Overall, after the system stabilizes, the hydrometeor mass partitioning in the domain is roughly 14% for cloud water, 4% for cloud ice, 14% for snow, 30% for hail/graupel and 38% for rain, so that the water phase (52%) slightly dominates the ice phase (48%). These percentages may be considered to reflect the characteristic microphysical structure of this maritime storm corresponding to the initial sounding profile.

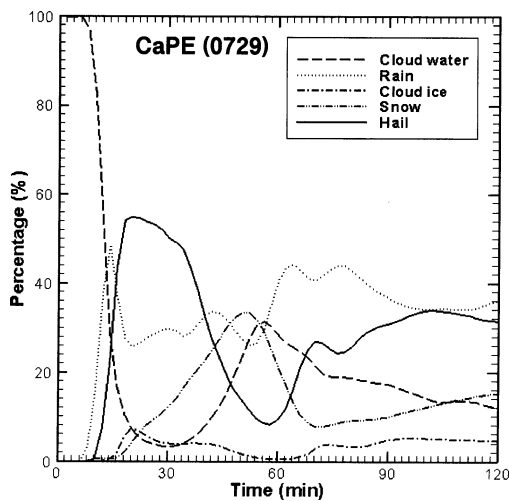


Fig. 9. Same as Fig. 8 except that the hydrometeor masses are plotted by percentage contributions.

The details of the relationships among various hydrometeors shown in Figs. 8 and 9 are examined below.

### 5.1.1. Rain

The rain sources and related percentage contributions are shown in Figs. 10a and 11a, respectively. Melting of snow (qsmr) and the concomitant shedding of collected unfrozen cloud water (qsacw) contribute less than 1% of the total, and hence are neglected in Fig. 11a. Much as in the Taipei case, warm microphysics dominates the first 10 min, with accretion overshadowing autoconversion as the first cell develops. This behavior also occurs during 40–60 min as the new cell develops. Around 20 min, precipitation loading and the fall of heavy ice particles to lower levels exert the same effects as for the Taipei storm near 16 min, greatly influencing the relative importance of the rain sources. The rain production due to collision and coalescence (qracw) abruptly decreases from 82% at 10 min to 2% at 46 min in response to the dissipation of initial storm. This process rebounds to 70% at ~60 min when the new cell is developing, then decreases to about 30% after the new system stabilizes at ~66 min.

Thus, this oscillation is highly related to initial storm growth. Collision and coalescence (qracw) are strong in the early stages, when the ice-phase hydrometeors are still in middle and upper levels, but then decrease rapidly in response to abundant hail/graupel falling through the melting level. This source (qracw) requires raindrops where the largest cloud water contents are. During 30–48 min, then, as the initial cell dissipates, the strong downdraft and weak updraft accelerate rain production from melting of hail/graupel (qhmlr), and decelerate the collision/coalescence (qracw) process.

After 16 min, the rain source is gradually dominated by the shedding (qshsr) and melting (qhmlr) of hail/graupel. Shedding parallels the maximum updraft evolution (Fig. 9) as the initial storm dissipates and the new system stabilizes. This process has a peak percentage of 68% at 26 min, then decreases to 4% at 54 min. During the quasi-steady stage, shedding (qshsr) averages 42% of the total rain production. Melting peaks at 78% at 48 min, when the initial cell dissipates and its total hail mass declines (Fig. 8). This high value is strongly related to the vigorous downdraft preceding dissipation. Due to the high subcloud temperatures, the falling hail/graupel melts to rain in this environment, thus contributing the largest rain source at the end of the initial cell. After 48 min when the new system first develops, melting decreases for lack of a hail/graupel source (Figs. 8 and 9) while collision/coalescence (qracw) is strong. After the new system becomes quasi-steady, melting (qhmlr) averages 28% of the total rain production rate, while melting and shedding of hail/graupel combine to contribute the bulk (70%).

Figs. 10b and 11b show the rain sinks and their related percentage contributions respectively. Accretion of supercooled raindrops by cloud ice to form snow (qiacr) is the main sink for rain in the first 10 min, but loses its dominance quickly as the hail/graupel mass grows (Figs. 8 and 9) and begins to precipitate out of the upper levels. A similar situation occurs after the new cell develops at 48 min; this sink grows to 30% at 60 min, but then decreases and stabilizes near 10% (Fig. 11b). Its peak is smaller at 60 min than at 8 min is because there are then more ice-phase hydrometeors of other types (Fig. 8). However, consumption by ice-phase hydrometeors still counts as the major sink of rainwater at 60 min, when the second storm system has just developed.

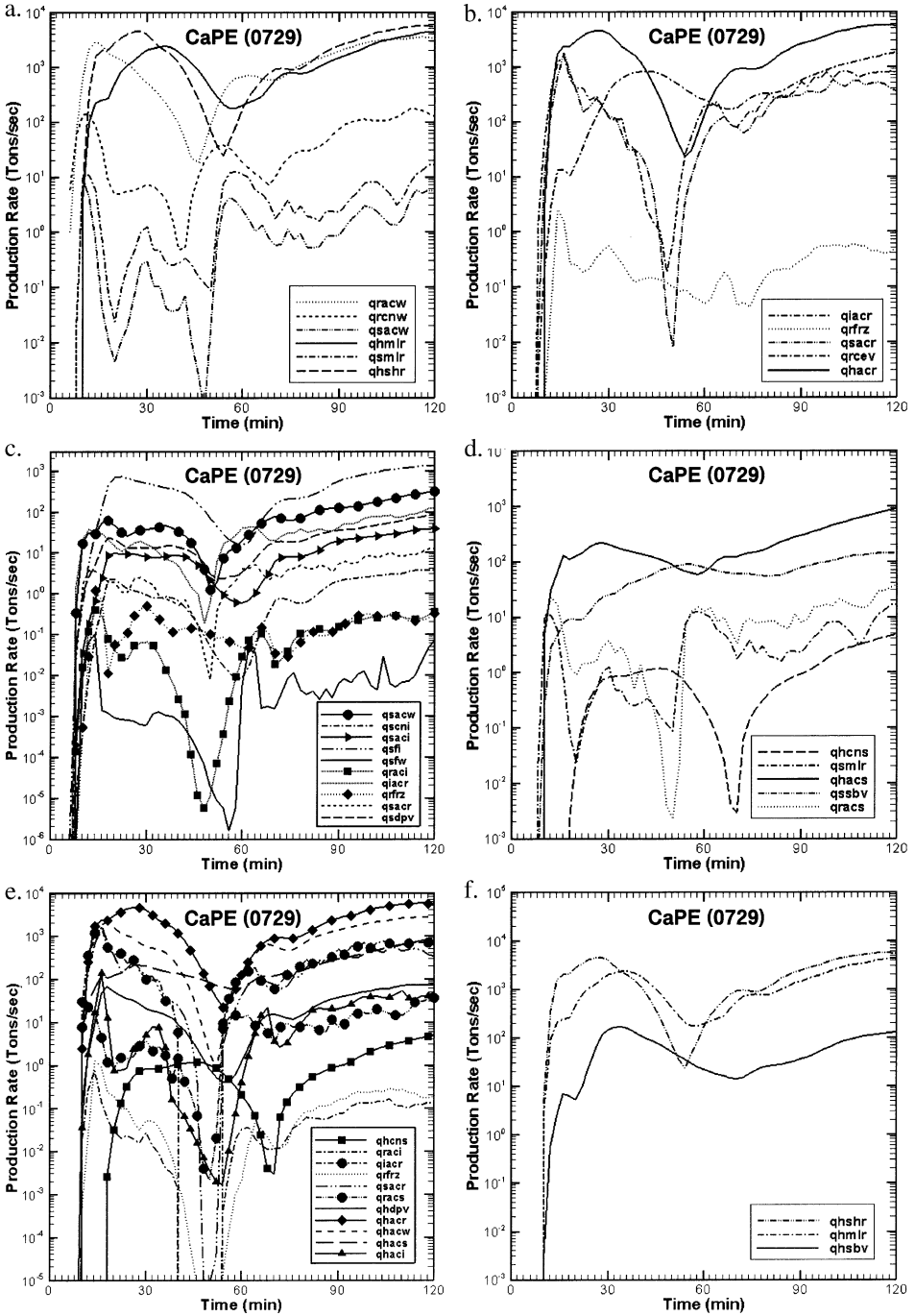


Fig. 10. Sources and sinks of each precipitating hydrometeor class for the CaPE, 29 July 1991 storm: (a) rain sources, (b) rain sinks, (c) snow sources, (d) snow sinks, (e) hail/graupel sources, (f) hail/graupel sinks.

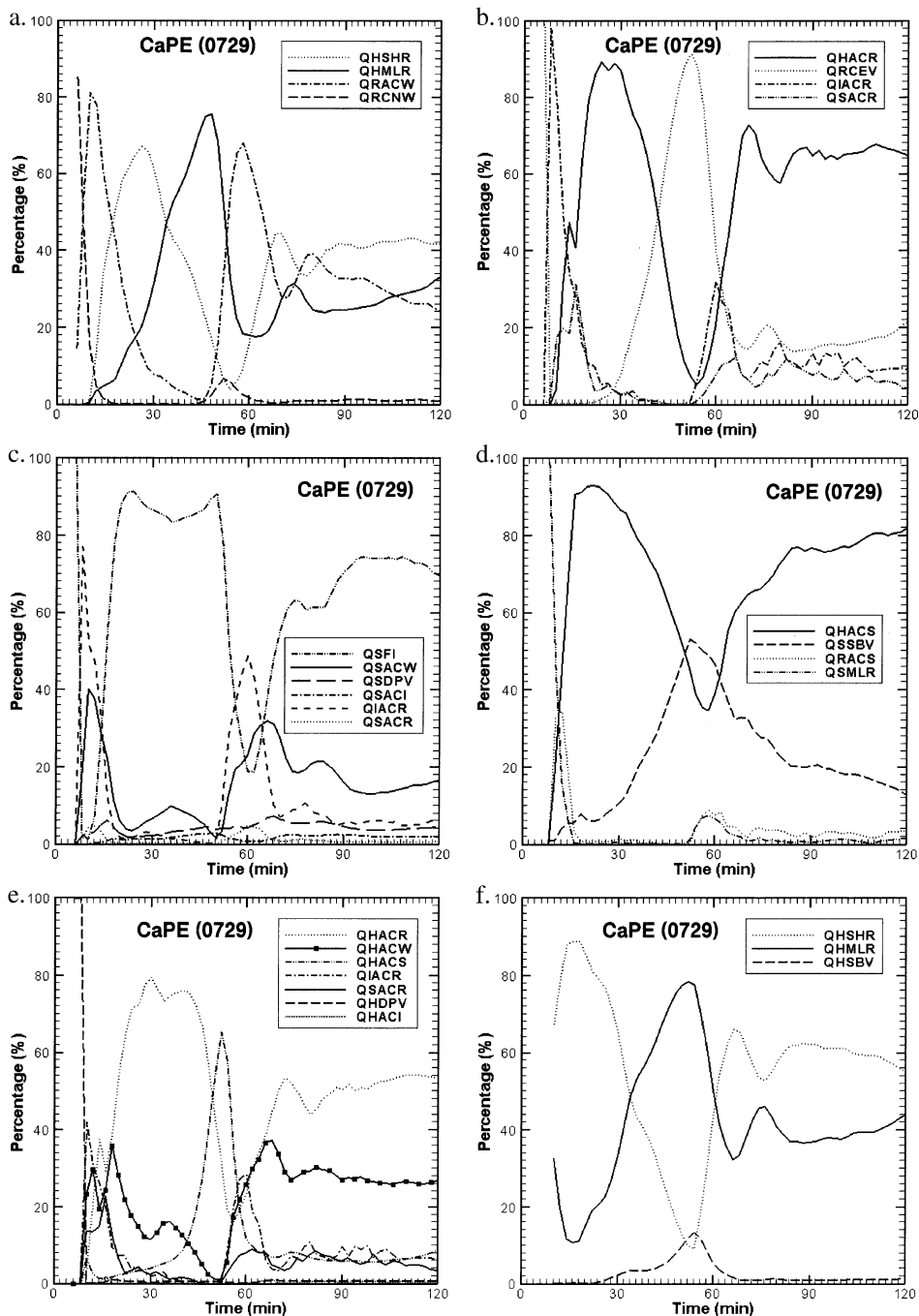


Fig. 11. Same as Fig. 10 except that the precipitating hydrometeor sources and sinks are plotted by percentage contributions.

Between 10 and 40 min when many hail/graupel particles first fall, their accretion of rain (qhacr) is the largest rain sink, paralleling the hail/graupel mass evolution (Figs. 8, 9). After the new storm system becomes quasi-steady, this process (qhacr) averages 66% of the total rain depletion rate. The next largest sink, averaging 18% of this total after stabilization, is evaporation of rain (qrcev). Very early, when the updraft speed is small and all hydrometeors in the domain are liquid (Figs. 8 and 9), evaporation is the only sink of rain (Fig. 11b), but then decreases rapidly as other hydrometeors grow to compete with the rain. The peak at 52 min (Fig. 11b) is caused by the dissipation of the initial storm, as large ice-phase hydrometeors precipitate out while small (light) ones remain in upper levels. Evaporation of rain (qrcev) also trends opposite to the accretion of rain by hail/graupel (qhacr). Because of the nearly saturated environment and weaker updraft (Fig. 3) to suspend the hail/graupel aloft, evaporation does not overshadow accretion of rain by hail/graupel. The other 6% of the rain depletion is mainly its accretion by snow to form hail/graupel (qsacr). A closer inspection of the curve reveals that accretion by snow (qsacr) and hail/graupel (qhacr) have the same trend, with some time lag. Because less snow is produced (Figs. 8,9), mostly in upper levels, and also because snow has smaller collision efficiencies for rain than the hail/graupel does, far less rain is accreted by snow (6%) than by hail/graupel (66%).

### 5.1.2. Snow

Figs. 10c and 11c show the snow sources and their percentage contributions, respectively. Processes with two or more orders of magnitude smaller than the primary sources are neglected in Fig. 11c, which shows that the leading snow source is Bergeron-Findeisen transformation of cloud ice to snow (qsfi). Its contribution increases significantly after 10 min, surpassing 90% around 20 min. When the cloud ice mass reaches its minimum in Fig. 8 (~60 min), this process (qsfi) does likewise, as the new cell begins to stabilize. After 66 min, the Bergeron-Findeisen process averages 70% of the total snow production, and parallels the maximum updraft after 60 min (Fig. 3). This implies that the updraft lifts the small water droplets from the low levels to the middle and upper levels (where cloud ice is abundant) as supercooled water. Because the supercooled droplets are small, accretion of snow is less efficient than vapor diffusion and the Bergeron-Findeisen process is the most dominant snow production mechanism.

The second largest snow source is accretion of cloud water (qsacw). For the new storm system, this process peaks at 32% of the total snow production at 66 min, and then decreases to average about 18% for the remaining time (Fig. 11c). The next largest snow source is cloud ice accreting rain (qiacr), at approximately one-third the rate that snow accretes cloud water (qsacw), averaging 6% overall.

Vapor deposition (qsdpv) occurs primarily in the updraft region where supersaturation with respect to ice is the greatest. After 68 min, it is the fourth largest source, with a 4% average contribution. This process varies only modestly through most of the simulation and is not affected by cell dissipation or development. The other two minor mechanisms, in which snow accretes rain (qsacr) and cloud ice (qsaci), together represent only 2% of the total snow production in the quasi-steady state.

Figs. 10d and 11d show the snow sinks and their related percentage contributions respectively. Because rain and hail/graupel are the two most abundant hydrometeors in the simulation (Figs. 8 and 9) and snow occurs mainly above the 0°C level with low terminal velocities, the main sink is accretion by hail/graupel (qhacs), averaging 76% of the total snow depletion rate during the quasi-steady stage (Fig. 11d). The decline of hail/graupel mass during ~30–60 min (Fig. 8) modulates this process, as does the renewed growth of hail/graupel mass after 60 min. Sublimation (qssbv), averaging 18% of the total sink, is the second largest contributor and is occurring primarily in and below the outflow anvil. During 40–80 min this process (qssbv) oscillates, with a peak at 52 min (Fig. 11d), because snow is more abundant than hail/graupel when the initial cell dissipates and the new system is stabilizing (Figs. 8 and 9). In the absence of hail/graupel in the upper levels, with less rain to deplete snow there, the major snow sink in this time period is sublimation (qssbv). Accretion of snow by rain to form hail/graupel (qgracs) near the 0°C isotherm, and the melting of snow (qsmr) below the melting level, are significant only in the first 16 min and when the new system is developing near 60 min. The last two processes, combined, contribute only 5% of the total snow depletion thereafter.

### 5.1.3. Hail/graupel

Figs. 10e and 11e, plotting the sources of hail/graupel and their related percentage contributions, respectively, show that hail/graupel is important to production and depletion of rain and depletion of snow. Accretional growth, including accretion of rain (qhacr), cloud water (qhacw) and snow (qhacs), is the major source of hail/graupel, averaging 84% of the total hail/graupel production rate after the new system stabilizes. Accretion of rain by cloud ice (qiacr) and snow (qsacr), along with accretion of snow by rain (qgracs), account for the other 16% of the total hail/graupel production rate.

After 68 min, the largest source of hail/graupel is accretion of rain (qhacr) in the lower region of the cloud, accounting for ~48% of the total production rate. This process parallels the mass production of rain (Fig. 9). Accretion of cloud water by hail (qhacw), is the second largest source, averages ~28% of the total production rate in the quasi-steady state. Because the volume and content of cloud water are directly related to the updraft intensity, accretion of cloud water evolves similarly to the maximum updraft after 68 min (Fig. 3). Accretion of snow (qhacs) averages only about 8% of the total hail/graupel production, mainly due to the relatively small amount of snow produced (Figs. 8 and 9) and the low collection efficiencies of hail for snow at the cold temperatures where snow is most abundant. Indirect accretional growth (qiacr, qsacr), followed by supercooling, increases with time as the convective system strengthens when rain is carried far aloft; it averages 10% of the quasi-steady total production rate for hail/graupel.

Between 12 and 48 min, accretion of rain (qhacr) in Fig. 10e is the major mechanism corresponding to the massive amount of hail/graupel in the domain (Figs. 8 and 9). Accretion of snow (qhacs) peaks at 54 min, when snow is the most abundant hydrometeor (Fig. 9).

Fig. 10f shows the three individual hail/graupel sinks. Sublimation is two orders smaller than the other sources except during ~40–60 min. The related percentage contributions are shown in Fig. 11f. As described previously, shedding (qshsr) and melting

(qhmlr) of hail/graupel are the major rain producers. Since rain is the most abundant hydrometeor after  $\sim 58$  min (Figs. 8 and 9), the main sinks of hail/graupel are evidently shedding and melting as well (Fig. 11f). In the quasi-steady state, the greatest single sink is shedding during wet growth, averaging 58% of the total depletion at steady state, when melting of hail to rain contributes around 40%. The loss of hail due to sublimation outside the updraft is significantly less than the other terms, accounting for merely 2% of the total depletion rate. Interestingly, shedding (qshsr) in Fig. 11f evolves similarly to the updraft in Fig. 3, and opposite to melting in Fig. 11f.

### 5.2. High Plains case :: CCOPE, 2 August 1981

Based on the raw average subcloud mixing ratios shown in Table 1, the High Plains cases have smaller water vapor supplies than the subtropical ones, despite similar surface temperatures. The resulting higher and colder cloud bases shown therein suggest that cold microphysical processes will dominate the hydrometeor production. We choose one High Plains case to illustrate these points.

Figs. 12 and 13 show the time evolution of the total hydrometeor mass and percentage, respectively. The time evolution of total condensate mass for each hydrometeor category is shown in Fig. 14, and related percentage contributions are shown in Fig. 15. Both hail/graupel and rain masses grow initially, decrease slightly when the system begins to stabilize at 34 min, and then increase again rapidly to 3200 KT for hail/graupel and slowly to 600 KT for rain at 90 min (Fig. 14). Overall, hail/graupel accounts for 44% of the total

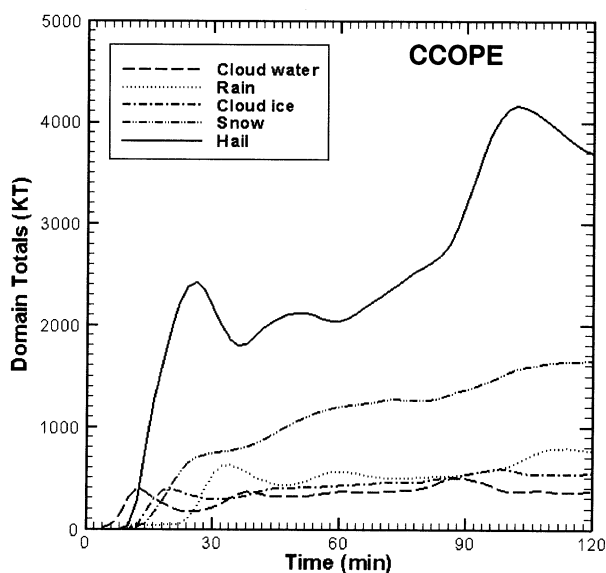


Fig. 12. Time evolution of simulated total condensate mass, integrated over the entire simulation domain ( $55 \times 55 \times 20 \text{ km}^3$ ), for both non-precipitating hydrometeors (cloud water and cloud ice) and precipitating ones (rain, snow and graupel/hail) in the simulated storms for the CCOPE storm.

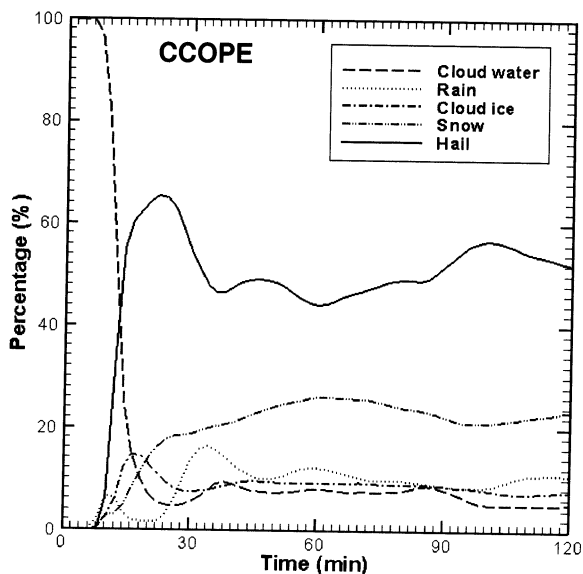


Fig. 13. Same as Fig. 12 except that the hydrometeor mass are plotted by percentage contributions.

water mass at 60 min and 48% at 90 min, while rain accounts for 13% and 9%, respectively (Fig. 15).

As expected, cloud ice appears before snow does, and has more total mass from 10 to 20 min. Subsequently, the snow mass exceeds, and grows faster than, the cloud ice mass (Fig. 1e). The snow mass increases from 400 KT at 20 min to approximately 1700 KT at 120 min. With the onset of cold microphysical processes, the total liquid mass varies relatively little with time (Fig. 14). The rain mass increases from 440 KT at 40 min to 780 KT at 120 min, while the cloud water mass is almost steady near 360 KT. Closer inspection of Fig. 1e reveals a time lag of ~10 min between cloud water and cloud ice maxima (or minima) for the same reason as in the NHRE case.

Once again, the increasing hydrometeor masses after 30 min reflect widening areal coverage rather than increasing precipitation rates. After the system stabilizes at ~34 min (spin-up time), the mass percentages (Fig. 15) average 7% for cloud water, 9% for cloud ice, 24% for snow, 49% for hail/graupel and 11% for rain. Thus, the liquid phase (18%) is far less abundant than the ice phase (82%). Microphysical processes responsible for the trends of these curves (Figs. 14 and 15) are covered in the following sections.

### 5.2.1. Rain

The individual rain sources and their related percentage contributions are plotted in Figs. 14a and 15a, respectively. The largest sources are melting of hail/graupel (qhmlr, 72%) and shedding of rain (qhshr, 19%) during wet growth, together accounting for 91% of the total rain production rate during the mature stage of the storm at 90 min (Fig. 15a). Lin et al. (1983) and Kubesh et al. (1988) have reported similar results for High Plains convective storms. Peaks in the melting and shedding of hail/graupel (Fig. 14a) occur ~5

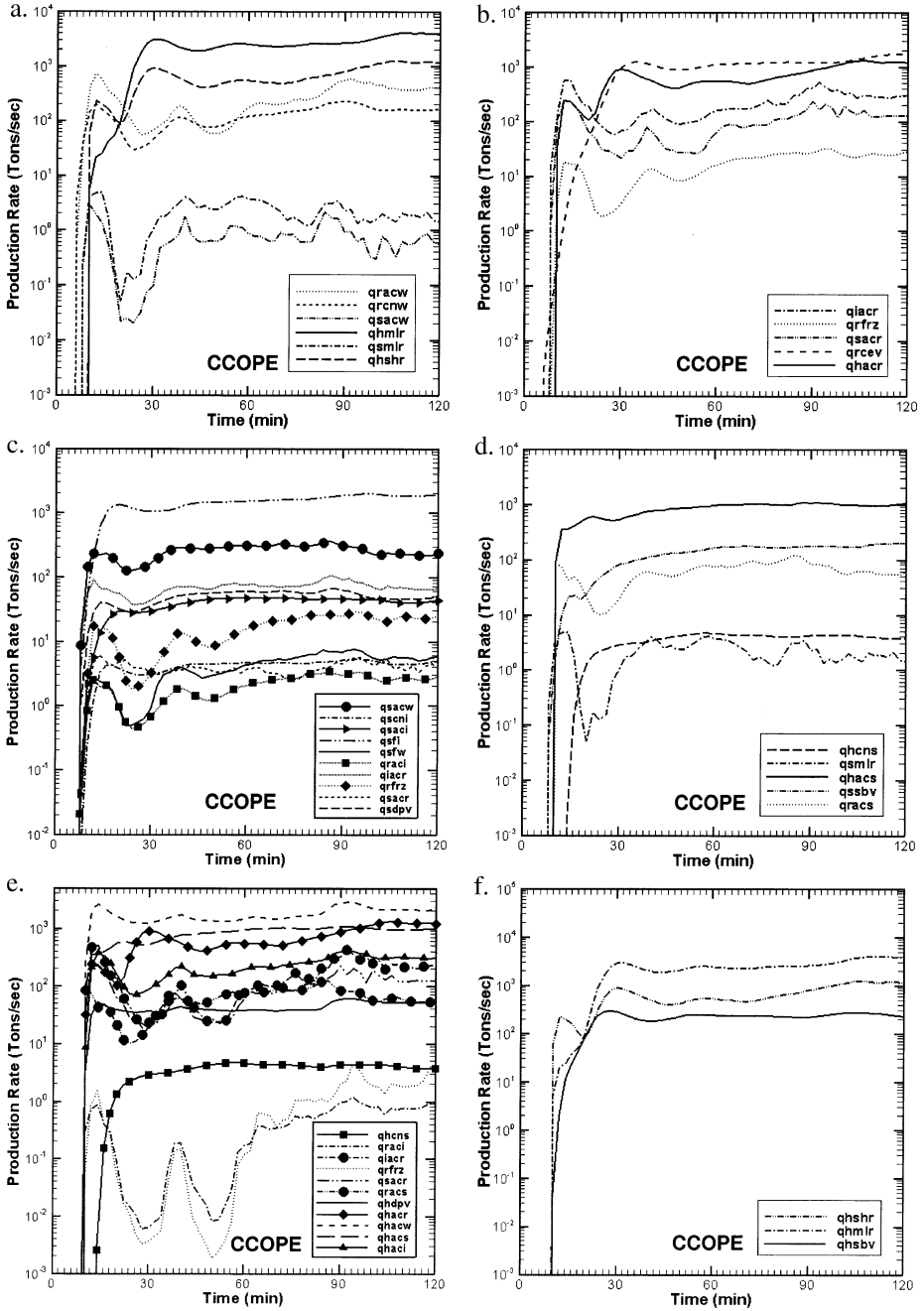


Fig. 14. Same as Fig. 10 except for the CCOPE storm of 2 August 1981.

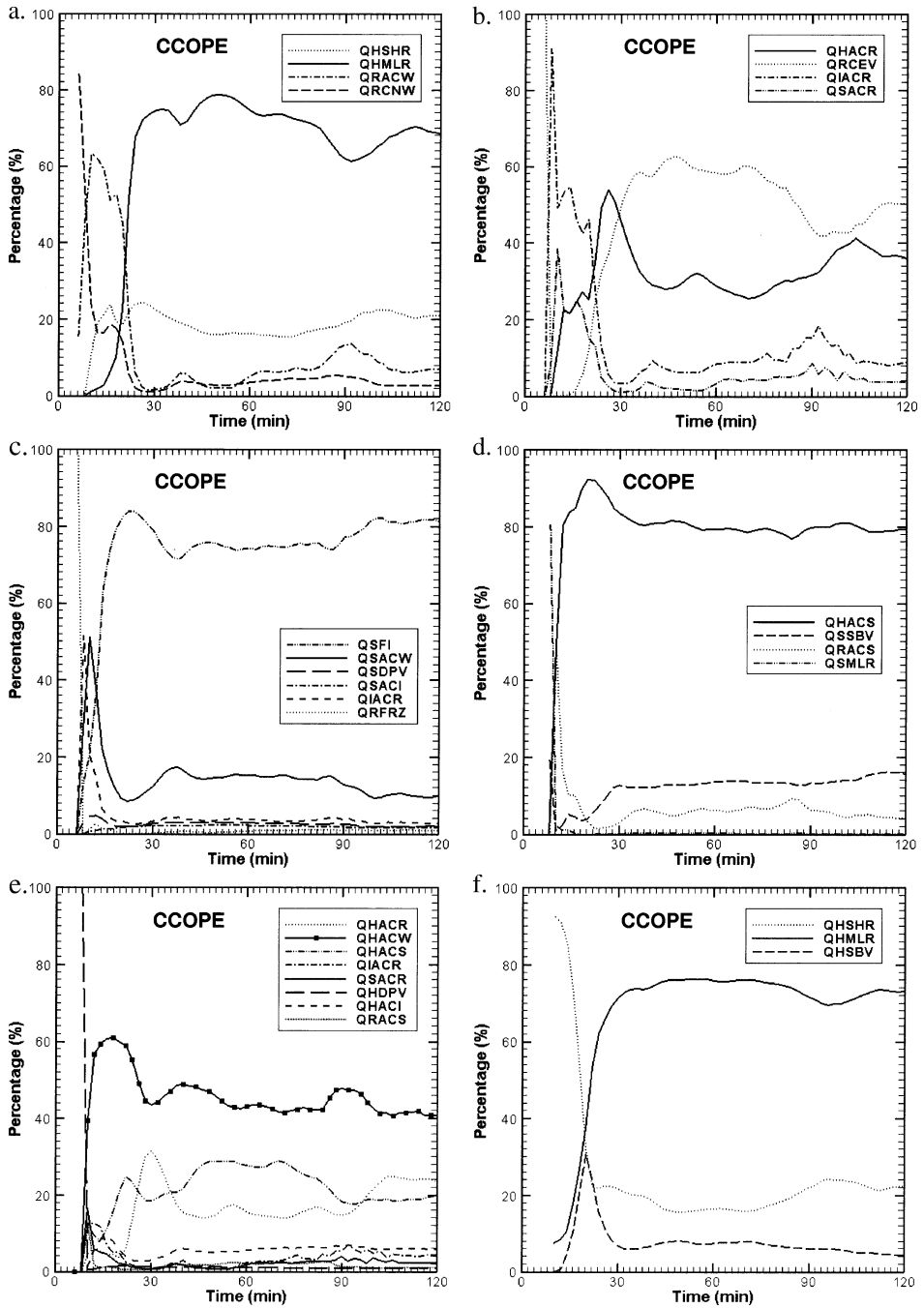


Fig. 15. Same as Fig. 11 except for the CCOPE storm of 2 August 1981.

min after maxima in the total hail/graupel mass (Fig. 12). Smaller but still significant sources of rain include accretion ( $q_{racw}$ ) and autoconversion of cloud water ( $q_{rcnw}$ ), accounting for 13% and 4.5% of the total rain production rate respectively at 90 min (Fig. 15a). These rates are relatively small for the same reason as in the NHRE case. Rain production from melting of snow ( $q_{smlr}$ ) and from the concomitant shedding of collected but unfrozen cloud water ( $q_{sacw}$ ) can be considered negligible, as their combined production rates are less than  $2 \text{ T s}^{-1}$  (Fig. 14a).

Figs. 14b and 15b show the individual rain sinks and the related percentage contributions respectively. Evaporation ( $q_{rcev}$ ) is initiated first but is overshadowed by cold microphysical processes when the updraft is stronger during 8–20 min. After the updraft decreases from its first peak at 15 min in response to precipitation loading, the large hydrometeors (rain and hail/graupel) fall from the relatively dry midlevels. Evaporation ( $q_{rcev}$ ) is the largest sink (40–62%) for rain during 30–120 min (Fig. 15b). When numerous hail/graupel particles fall out, they accrete rain and contribute the second largest sink ( $q_{hacr}$ ). During the quasi-steady state (after 34 min), these two processes together average 84% of the total rain depletion rate.

The next largest sink, contributing 11%, is accretion of rain by cloud ice ( $q_{iacr}$ ) above the  $0^\circ\text{C}$  isotherm to form snow or hail/graupel. Raindrops at these levels initially form and grow by autoconversion ( $q_{rcnw}$ ) and accretion ( $q_{racw}$ ) of cloud water, accounting for about 19% of the cloud water depletion rate (not shown). The accretion of rain by snow to form snow or hail/graupel ( $q_{sacr}$ ) is a smaller (4% overall) yet nevertheless important rain sink, while freezing of raindrops to form snow or hail/graupel ( $q_{rfrz}$ ) is less significant.

### 5.2.2. Snow

Figs. 14c and 15c show the individual snow sources and their related percentage contribution, respectively. The greatest snow production mechanism is the Bergeron-Findeisen process ( $q_{sfi}$ ), which increases significantly after 6 min and reaches  $\sim 84\%$  of the total snow production rate around 20 min (Fig. 15c), averaging 78% of this total after stabilizing at 34 min. The reasons for this strong dominance are much the same as in the NHRE storm.

The second largest snow source is direct accretion of cloud water ( $q_{sacw}$ ), mostly at temperatures of  $-10$  to  $-20^\circ\text{C}$ . Paralleling the trend of the cloud water mass, this process reaches its maximum percentage (50%) at 10 min (Fig. 15c), and then decreases to an average of about 14% overall for the remaining time. The next largest snow source after stabilization is cloud ice accreting rain ( $q_{iacr}$ ); despite reaching a maximum 52% at 8 min, it decreases quickly to stabilize at  $\sim 4\%$  by 20 min. A secondary snow source is vapor deposition ( $q_{sdpv}$ ), primarily in updraft regions where supersaturation with respect to ice is the greatest, and accounts for 2% of the total snow mass production. Thus, these four processes together account for 98% of the total.

Figs. 14d and 15d show the individual snow sinks and their related percentage contributions, respectively. The largest snow sink is its accretion by hail/graupel ( $q_{hacs}$ ), stabilizing at  $\sim 80\%$  of the total snow depletion rate (Fig. 15d). This process evolves similarly to the hail/graupel mass percentage in Fig. 13. Sublimation ( $q_{ssbv}$ ), generally the second largest sink of snow, occurs primarily in and below the outflow anvil and accounts for 14% of the total snow depletion rate. Accretion of snow by rain to form hail/graupel ( $q_{racs}$ ), in the

lower regions of the cloud near the 0 °C isotherm, accounts for most of the remaining 6%. Aggregation of snow to form hail (qhchs) and the melting of snow to rain (qsmr) are two orders of magnitude less than the other sinks (Fig. 14d) and therefore negligible.

### 5.2.3. Hail/graupel

Figs. 14e and 15e, showing the individual hail/graupel sources and their related percentage contributions, respectively, reconfirm that hail/graupel is important to the production and depletion of rain and snow. Accretional growth modes (qhacw, qhacr, qhacs, qhaci) are the largest source terms, together contributing 91% of the total hail/graupel production (Fig. 15e). Also, these rates follow trends nearly identical to the mass percentages of each hydrometeor being accreted (Fig. 13).

Fig. 15e also shows that the largest source is accretion of cloud water (qhacw), accounting for ~44% of the total hail/graupel production rate. Accretion of snow, contributing 23%, is the second largest source. Accretion of rain by hail/graupel (qhacr), in and beneath the lower regions of the cloud, is the third largest source, averaging an 18% contribution. Between 40 and 90 min, accretion of rain diminishes because less hail falls into the melting layer as the updraft increases, but this accretion then increases rapidly when updraft velocities stabilize and more hail falls out again. Accretion of cloud ice by hail/graupel (qhaci) is less important, contributing 6% overall, as little cloud ice is located in the warmer midlevel regions of the cloud.

Collisions between snow and rain (qsacr, qracs), near the 0 °C isotherm, constitute the largest secondary hail/graupel sources (5% total), while freezing of raindrops (qfrz) is negligible in comparison. These sources strengthen with the storm, peaking during its most intense phase when rain is carried highest into the colder altitudes. Updraft loading by numerous hail/graupel particles is largely responsible for depleting the cloud water (Figs. 12 and 13) and weakening the updraft after 20 min. Above the 0 °C isotherm, deposition of water vapor (qhdpv) is more than an order of magnitude smaller than the accretion terms.

Figs. 14f and 15f show the individual hail/graupel sinks and their related percentage contributions respectively. Melting of hail to rain (qhmlr) accounts for ~75% of the total hail depletion rate, while shedding during wet growth (qhshr) accounts for about 20%. Finally, sublimation (qhsub) is significantly less than the other sinks, contributing only 5%.

## 6. Discussion

The microphysical processes evolving in two of the six simulated storms have been described clearly in previous sections, directing considerable effort into comparing these processes in warm-season thunderstorms for High Plains versus humid subtropical regions. The remaining four cases contain similar information and have been subject to similar comparisons. These comparisons are necessary for further understanding of the controlling mechanisms that account for the differences between the storms in these two areas. The similarities and differences between the microphysical processes in each are discussed in this section.

One important fact worth mentioning here is that the model results in the spin-up period (the first 40–50 min) are usually unrepresentative of the general condition of the storm. The numbers and conclusions presented below are based on the results after the simulated storms have reached quasi-steady state and hence more representative.

### 6.1. Domain totals

Derived from the time series (such as Figs. 9 and 13), Table 2 shows the time-averaged domain-integrated mass percentage statistics for each hydrometeor class during the quasi-steady stages of all six thunderstorm simulations. The results show that more than 80% of the total hydrometeor mass is precipitation (rain, snow, graupel/hail) in both the High Plains and the humid subtropics. It is also clear that the ice-phase hydrometeors (cloud ice, snow and hail/graupel) are strongly dominant in the High Plains cases (~80%), but not in the subtropical ones (~50%). Both sets of storms produce considerable graupel/hail aloft, but appreciable hail/graupel reaches the ground only in the High Plains storms, melting almost completely before reaching the ground in the subtropical cases. Table 1 shows that the High Plains environments generally have higher surface temperature and drier low-level air than the subtropical ones. Also, the soundings show that the High Plains environments have nearly dry-adiabatic lapse rates up to ~400 mb and generally have higher and colder LCLs. Note that the wet bulb zero level, where the lowest temperature attainable through isobaric evaporation of water is 0 °C, is lower in the High Plains, especially for the CCOPE case.

Close inspection of Table 2 reveals that the partitioning between precipitating and non-precipitating hydrometeors differs very little among the three High Plains cases. Also, the combined hail/graupel and snow percentages are nearly the same for each High Plains case after stabilization. The appreciable differences between them involve the separate percentages of hail/graupel and snow. Table 2 show that hail contributes a higher share in CCOPE than in the other two cases, increasing slightly during 60–100 min. For the other two High Plains storms, the contributions of hail decrease slightly in the same time. The percentages of snow in the weaker High Plains storm cases are more than in the

Table 2

Time-averaged partitioning of the domain-integrated hydrometeor masses during the quasi-steady stage of each simulated storm

	High Plains (%)			Subtropics (%)		
	CCOPE	NHRE	NDTP	Taipei	CaPE (07/29)	CaPE (08/15)
Cloud	7	9	9	8	14	11
Rain	11	13	12	35	38	32
Ice	9	6	6	5	4	5
Snow	24	27	36	18	14	16
Hail	49	45	37	34	30	36
Precipitates	84	85	85	87	82	84
Non-precipitates	16	15	15	13	18	16
Snow + Hail	73	72	73	52	44	52
Ice phases	82	78	79	57	48	57
Water phases	18	22	21	43	52	43

Table 3  
Rankings of the domain-integrated individual sources and sinks of rain

		High Plains			Subtropics		
		CCOPE	NHRE	NDTP	Taipei	CaPE (07/29)	CaPE (08/15)
Production	qhshr	2	2	2	1	1	1
	qhmlr	1	1	1	2	2	2
	qracw	3	3	5	3	3	3
	qrnw	4	5	4	4	4	4
	qsmrl	5	4	3	5	5	5
	qsacw	6	6	6	6	6	6
Depletion	qhacr	2	2	2	1	1	1
	qrcev	1	1	1	2	2	2
	qiacr	3	3	3	3	3	3
	qsacr	4	4	4	4	4	4
	qrfrz	5	5	5	5	5	5

The ranking is according to the time-averaged magnitude during the quasi-steady stage of each simulated storm. The lower the number, the more important the process is.

CCOPE case, especially for the NDTP storm. The subtropical cases have comparable or larger percentages for rain versus hail/graupel. Table 2 shows snow percentages about half of those for the High Plains, as well as more cloud water, less cloud ice, and much less precipitating ice (snow and hail/graupel).

## 6.2. Rain

Each individual microphysical source and sink of rain is ranked in Table 3 according to its time-averaged magnitude during the quasi-steady phase of each storm simulated (for acronyms in Tables 3–5, please see Table 6). The lower the number, the more important

Table 4  
Same as Table 3, except for snow instead of rain

		High Plains			Subtropics		
		CCOPE	NHRE	NDTP	Taipei	CaPE (07/29)	CaPE (08/15)
Production	qsfi	1	1	1	1	1	1
	qsacw	2	2	2	2	2	2
	qsdpv	3	3	3	3	4	3
	qsaci	5	4	4	4	5	5
	qiacr	4	5	5	5	3	4
	qsacr	8	6	6	6	6	6
	qseni	7	7	7	7	7	7
	qraci	10	8	9	8	8	8
	qrfrz	6	9	8	9	9	9
	qsfw	9	10	10	10	10	10
Depletion	qhacs	1	1	1	1	1	1
	qssbv	2	2	2	2	2	2
	qracs	3	4	4	3	3	3
	qsmrl	5	3	3	4	5	4
	qhens	4	5	5	5	4	5

Table 5  
Same as Table 3, except for hail/graupel instead of rain

		High Plains			Subtropics		
		CCOPE	NHRE	NDTP	Taipei	CaPE (07/29)	CaPE (08/15)
Production	qhacr	2	3	3	1	1	1
	qhacw	1	2	2	2	2	2
	qhacs	3	1	1	3	3	3
	qiacr	4	9	9	4	4	4
	qsacr	6	6	8	5	5	5
	qhdpv	7	4	4	6	6	6
	qhaci	5	5	5	7	7	8
	qracs	8	7	6	8	8	7
	qhcons	9	8	7	9	9	9
	qrfrz	11	10	10	10	10	10
Depletion	qraci	10	11	11	11	11	11
	qshsr	2	2	2	1	1	1
	qhmlr	1	1	1	2	2	2
	qhsbv	3	3	3	3	3	3

the process. Clearly, shedding (qshsr) and melting (qhmlr) of hail/graupel are the main rain sources in all cases. Fig. 16 shows the time evolution of each rain source in all six cases. Shedding and melting of hail compose about 90–97% of the rain production in the High Plains cases. In the subtropics, accretion of cloud water is the third most important source of rain.

Shedding of hail (Fig. 16a) is clearly the leading subtropical rain source, contributing 42–48%, somewhat more than melting (30–40%, Fig. 16b). By contrast, melting is the most dominant High Plains rain source, contributing 66–82%. These differences can be easily seen from the vertical cross-sections of the hydrometeor and wind fields. Detailed examination of the rain and hail fields therein shows that the maximum hail mixing ratios in the High Plains are generally higher up than, and well separated from, the rain below. Meanwhile, the heaviest hail concentrations in the subtropics are inside or near the rain area, with more supercooled droplets than in the High Plains cases. This indicates that most hail produced in the subtropical thunderstorms comes from accretion of rain and cloud water. Due to the relatively warm rain and cloud water and weak low-level updrafts in the subtropical storms, the accreted water has no time to freeze on the hail surface and is shed out when the hail falls. In addition, the hail core in the subtropics is far from the updraft core, and in weaker updraft than in the High Plains cases. Because hail/graupel is assumed to follow an inverse exponential size distribution in WISCDYMM, hail/graupel particles at lower levels are larger in the subtropical cases than in the High Plains storms. When the larger hail/graupel particles fall in the updraft, their surfaces melt and the surface water is ejected by the flow as rain before the particles melt completely. This is why the main subtropical rain source is from shedding of hail (Fig. 16a). In the High Plains, by contrast, most of the hail below the freezing level is sufficiently small to be carried aloft in the updraft. When hail passes through the warmer low levels, no strong wet growth occurs. Few droplets are collected on the surface of the hail, and the relative flow is weaker. Accordingly, the falling hail/graupel melts without much shedding. Thus, the rain

Table 6  
Definition of acronyms for microphysical processes

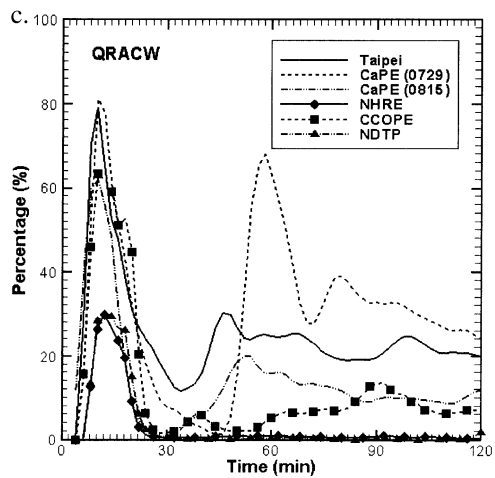
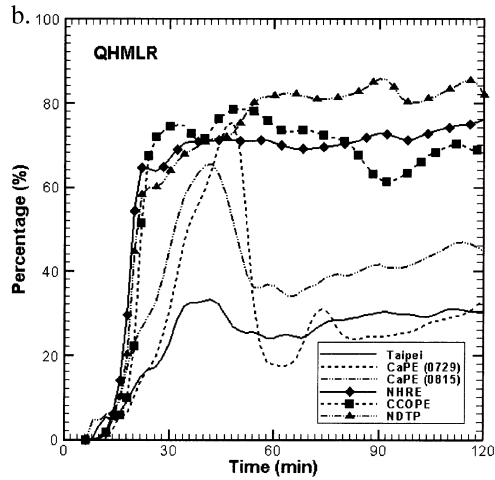
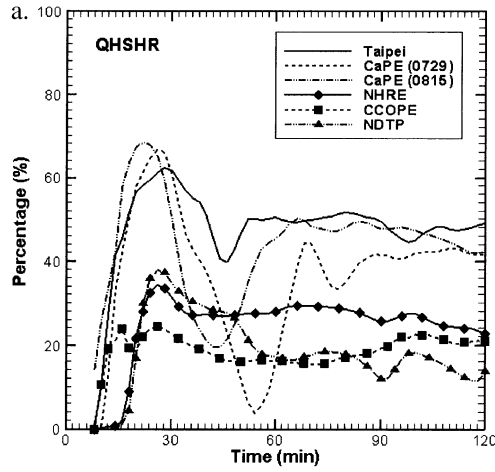
Acronym	Process
qhaci	Accretion of cloud ice by hail
qhacr	Accretion of rain by hail
qhacs	Accretion of snow aggregates by hail
qhacw	Accretion of cloud water by hail
qhcev	Condensation/Evaporation of vapor to/from wet hail
qhens	Autoconversion of snow to hail
qhdpv	Vapor deposition to hail
qhmlr	Melting of hail to rain
qhsbv	Vapor sublimation from hail
qhshr	Rain water shed from hail
qhspait	Secondary production I of cloud ice from hail
qhspbit	Secondary production II of cloud ice from hail
qiacr	Accretion of rain by ice to form snow or hail
qiaw	Accretion of cloud water by cloud ice
qiint	Nucleation of pristine cloud ice
qimlw	Melting of cloud ice to cloud water
qivds	Vapor Deposition/Sublimation to/from cloud ice
qraci	Accretion of cloud ice by rain to form snow or hail
qracs	Accretion of snow by rain to form snow or hail
qracw	Accretion of cloud water by rain
qrcev	Evaporation of rain
qrcnw	Autoconversion of cloud water to rain
qrfiz	Probabilistic freezing of rain to form snow or hail
qsaci	Accretion of cloud ice by snow
qsacr	Accretion of rain by snow to form snow or hail
qsacw	Accretion of cloud water by snow
qscv	Condensation/Evaporation of vapor to/from wet snow
qscni	Autoconversion of cloud ice to snow
qsdpv	Vapor deposition to snow
qsfi	Bergeron process, transfer of cloud ice to snow
qsfw	Bergeron process, transfer of cloud water to snow
qsmr	Melting of snow to rain
qssbv	Vapor sublimation from snow
qsspait	Secondary production I of cloud ice from snow
qsspbit	Secondary production II of cloud ice from snow
qvcnd	Condensatio/Deposition to/on cloud water/cloud ice
qvcs	Evaporation/Sublimation of cloud water/cloud ice
qwfzi	Homogeneous freezing of cloud water to cloud ice

produced in the High Plains storms comes mostly from melting (Fig. 16b) instead of shedding.

Another important source of rain is accretion of cloud water (qracw). Because collision and coalescence are involved, this process contributes significantly only if the rain

---

Fig. 16. Superimposed time series in all six storm simulations for the following rain sources (see text for their microphysical meanings): (a) qhshr, (b) qhmlr, (c) qracw. Curves with and without symbols along them are for the High Plains and humid subtropical cases respectively, with brief symbolic designations of each case in the legend boxes.



intercepts a region of large cloud water content. In the subtropical cases, relatively high freezing levels and low cloud bases leave much of the cloud water unfrozen. Smaller rain droplets inside the subtropical clouds are thus correspondingly more apt to grow instead of freezing, so that accretion of cloud water contributes 13–30% of the rain production in the subtropics but much less in the High Plains.

The sinks of rain are shown in Fig. 17. Accretion of rain by hail (qhacr; Fig. 17a) and evaporation of rain (qrcev; Fig. 17b) account for more than 90% of the rain depletion in all cases, as reflected in the rankings (Table 3). Because rain exists mostly at lower levels evaporation and collection by the larger hydrometeors should be dominant sinks. As discussed previously in regard to rain production, abundant hail exists at lower levels in the subtropical cases. When hail falls through these levels, it undergoes melting and accretion. Because of the nearly saturated environment, weaker updrafts in which to suspend the hail/graupel aloft, higher collection efficiencies for larger hail/graupel, and the strong overlap of rain and hail regions, accretion of rain by hail (qhacr) is a more important rain sink in the subtropics (>60%) than in the High Plains (<40%), as shown in Fig. 17a. But in the High Plains, because of the drier environment and smaller overlap of rain and hail, evaporation of rain (qrcev) is its main sink (>50%), as seen in Fig. 17b. In addition, because the midlevels are warmer in the subtropics than in the High Plains, supercooled raindrops are apt to survive and collide with snow and cloud ice before autoconversion. Therefore, depletion of rain due to accretion by cloud ice (qiacr; Fig. 17c) and snow (qsacr; Fig. 17d) and is more important in the subtropics than in the High Plains, where the freezing of rain to hail (qfrz) is also evident (Fig. 17e).

### 6.3. Snow

Table 4 ranks each individual microphysical source and sink of snow. The rankings are largely similar for the subtropical and High Plains cases. Bergeron transfer of cloud ice to snow (qsfi, Fig. 18a), accretion of cloud water (qsacw, Fig. 18b), deposition of vapor (qsdpv, Fig. 18c) and accretion of cloud ice (qsaci, Fig. 18d) account for more than 90% of the time-averaged snow production in all cases during their quasi-steady stages (Fig. 18). The Bergeron process (qsfi) is the leading mechanism (>50%), and is more dominant in the subtropics (>60%) than in the High Plains, except for the CCOPE supercell case. Due to colder midlevel temperatures and higher cloud bases in the High Plains, accretion of cloud water (qsacw) is evidently more important there (>30%) than in the subtropics (<20%), where most cloud water goes into raindrop growth (qracw). The colder High Plains environment aloft also leads to less vapor near the snow particle surface and enhances the vapor deposition (qsdpv) in the High Plains cases (>9%) versus the subtropics (<6%) except in the CCOPE case, as seen in Fig. 18c. Accretion of ice (qsaci) accounts for less than 4% of the snow production (Fig. 18d). Except the severe cases of Taipei (~3.7%) and CCOPE (2%), this process is more important in the High Plains (~3.5%) than in the subtropics (~2%).

The sinks of snow are plotted in Fig. 19. Accretion by hail (qhacs, Fig. 19a) and sublimation to water vapor (qssbv, Fig. 19b) account for more than 90% of the total depletion. The former process comprises more than 75% in both the High Plains and the subtropics. Sublimation mainly occurs beneath the anvil, and is highly dependent on the

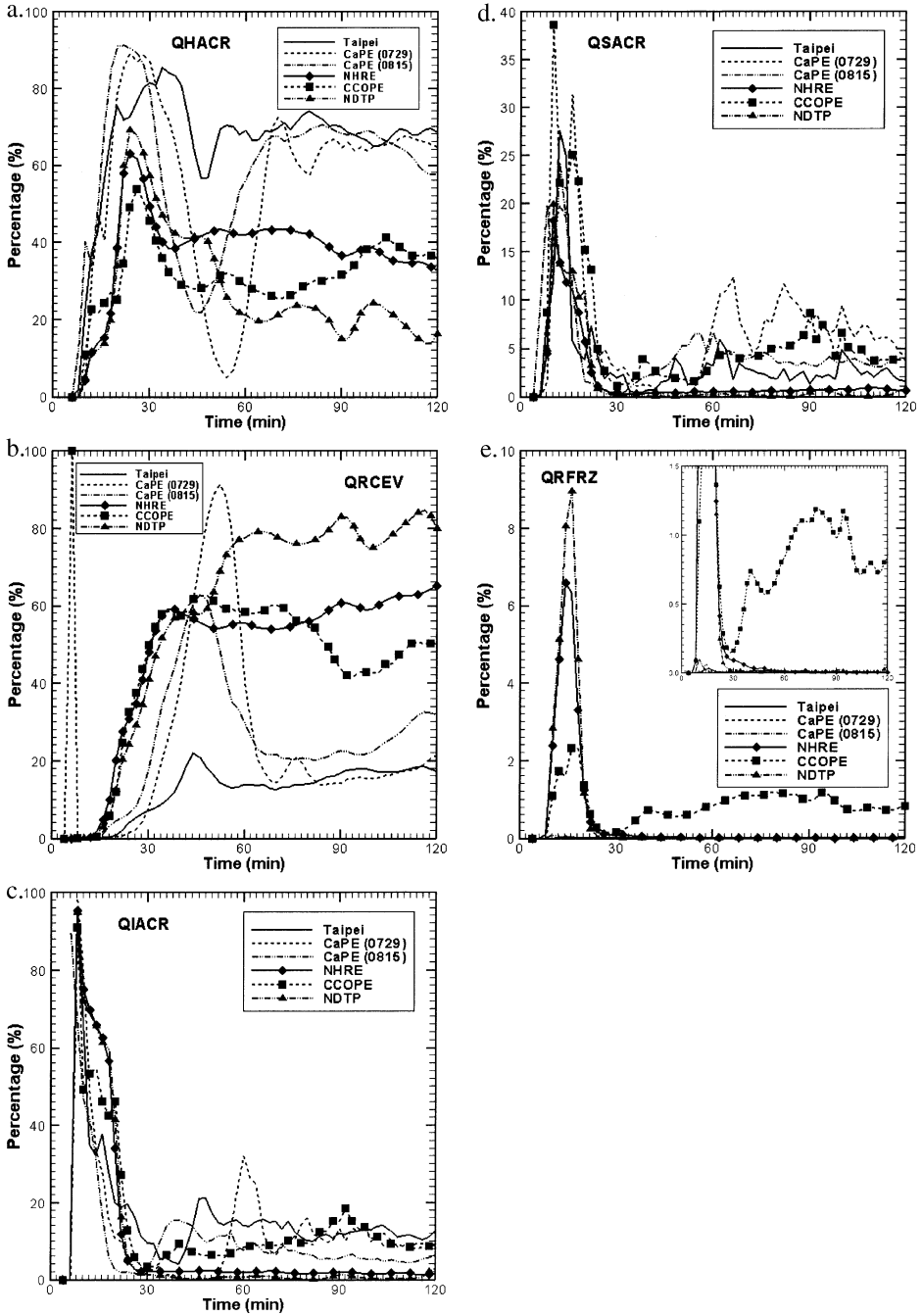


Fig. 17. Superimposed time series in all six storm simulations for the following rain sinks (see text for their microphysical meanings): (a) qhacr, (b) qrcev, (c) qiacr, (d) qsacr, (e) qrfrz. Legends are as in Fig. 16. Inside panel (e), smaller panel is added for clearer resolution of the very small percentage contributions shown in the main panel.

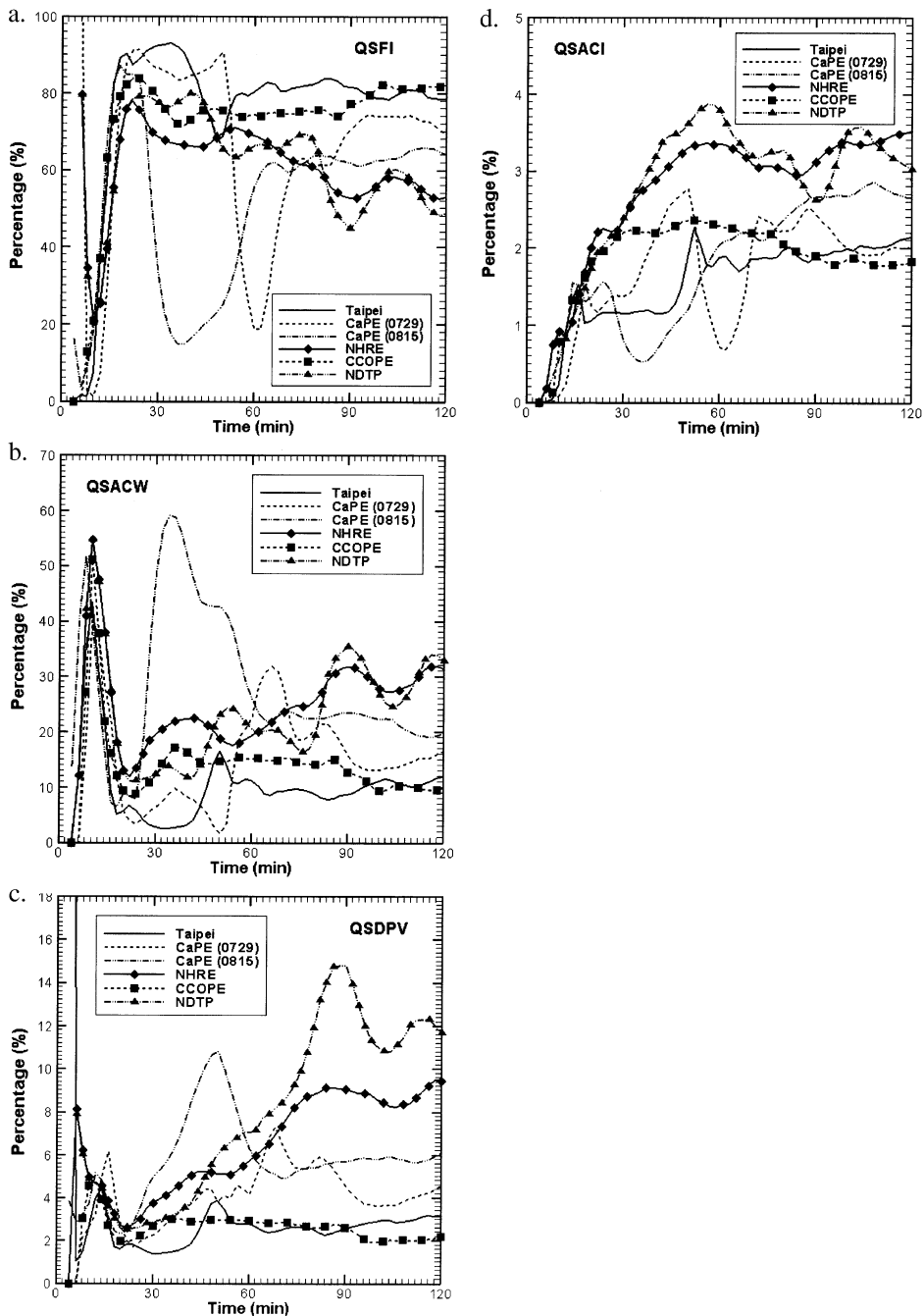


Fig. 18. Superimposed time series in all six storm simulations for the following snow sources (see text for their microphysical meanings): (a) qsfi, (b) qsacw, (c) qsdpv, (d) qsaci. Legends are as in Fig. 16.

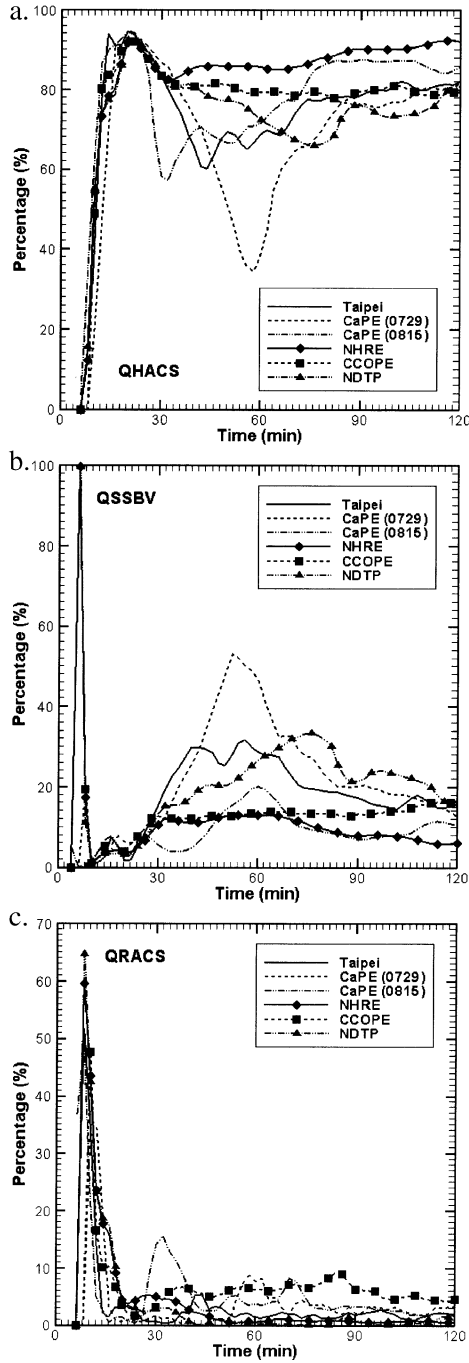


Fig. 19. Superimposed time series in all six storm simulations for the following snow sinks (see text for their microphysical meanings): (a) qhacs, (b) qssbv, (c) qracs. Legends are as in Fig. 16.

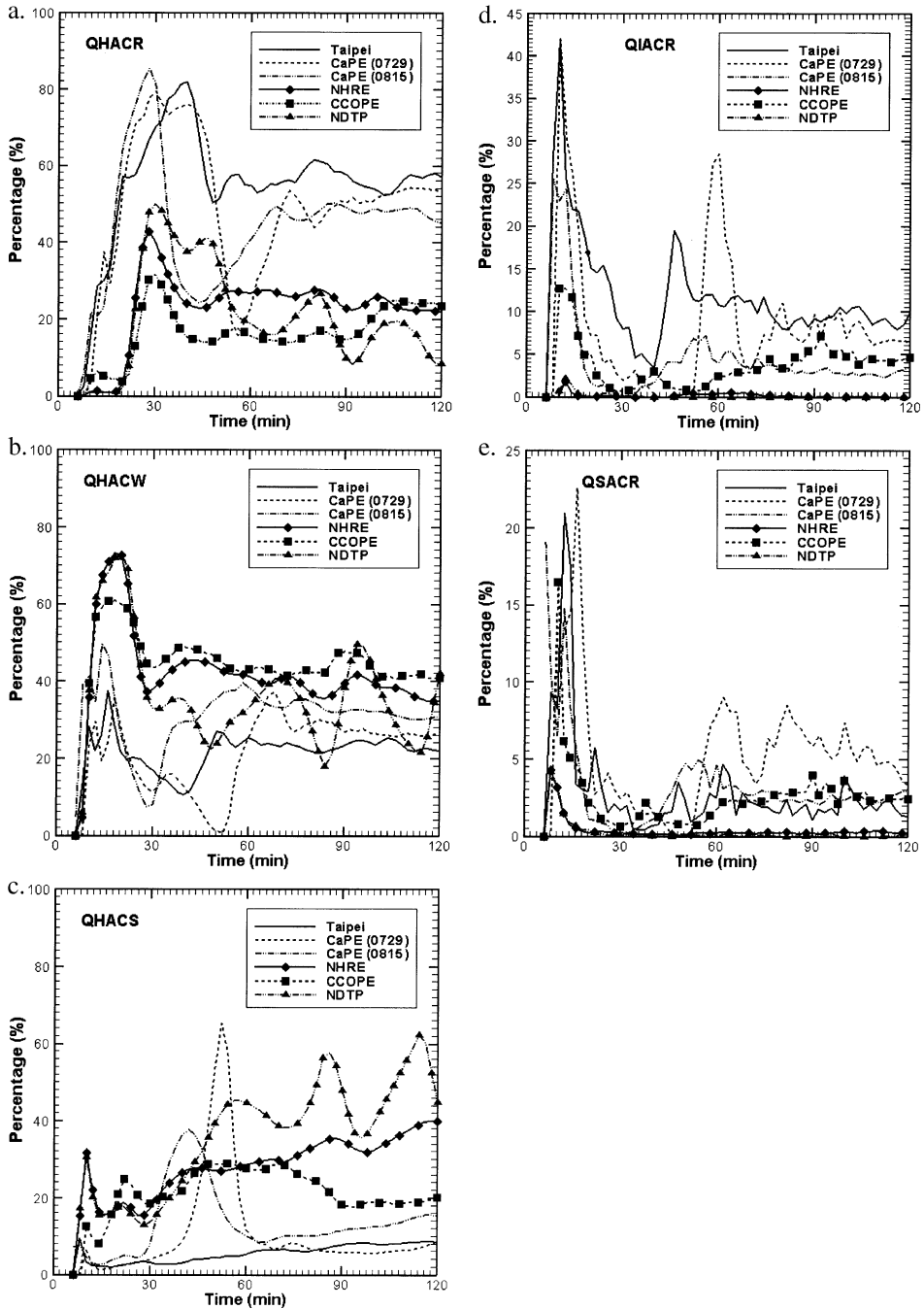


Fig. 20. Superimposed time series in all six storm simulations for the following hail/graupe sources (see text for their microphysical meanings): (a) qhacr, (b) qhacw, (c) qhacs, (d) qiacr, (e) qsacr. Legends are as in Fig. 16.

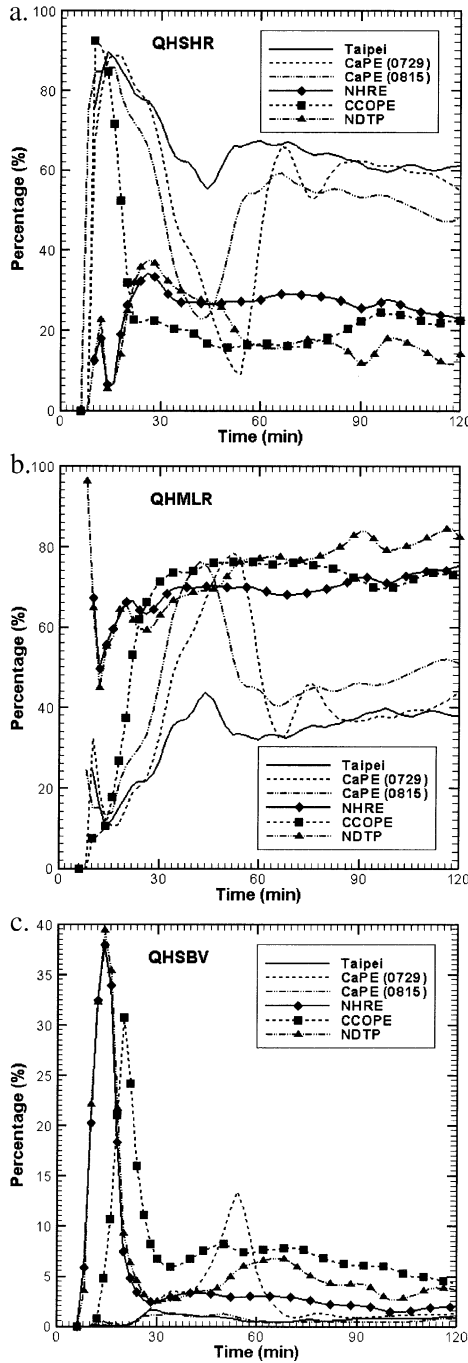


Fig. 21. Superimposed time series in all six storm simulations for the following hail/graupel sinks (see text for their microphysical meanings): (a) qshsr, (b) qhmlr, (c) qhsbv. Legends are as in Fig. 16.

spreading rate of snow. Therefore, the trends are mixed (Fig. 19b). Because the rain percentages are higher and the midlevels are warmer in subtropics, supercooled raindrops are likelier to be carried up to collide with snow instead of freezing, as discussed previously. Accretion of snow to form hail/graupel (qgracs) contributes an appreciable snow sink in the subtropical cases (Fig. 19c).

#### 6.4. Hail/graupel

Each individual microphysical source and sink of hail/graupel is ranked in Table 5. At first glance, the rankings appear broadly similar in both the High Plains and subtropical simulations, but some significant contrasts occur among the three leading sources. Fig. 20 plots the percentage contributions for the individual processes in each experiment. Accretion dominates all cases. Because hail/graupel is distributed in a deep layer, the accreted hydrometeors are mainly rain at low levels and cloud ice at high levels, as clearly shown in Fig. 20a–c, where the importance of the processes migrates between the High Plains and subtropics. The trends are highly related to hydrometeor production and distribution, as well as the ambient temperature.

Table 5 shows that cloud water and rain are the most important hydrometeors in the production of hail in the subtropics, versus cloud water and snow in the High Plains. As we described previously for the rain sources, rain penetrates well above the freezing level and highly overlaps the hail distribution in the subtropics, with little separation between the rain and hail cores. With lift from the updraft, many supercooled raindrops are collected by the hail, providing the leading source (>48%) of hail production, in contrast to the High Plains cases (<25%), as plotted in Fig. 20a. Because hail accretes cloud water less efficiently than it does rain, accretion of cloud water (qhacw) contributes a smaller percentage (<30%) in the subtropics than the accretion of rain (qhacr). In the High Plains, less rain penetrates above the freezing level, midlevels are colder and the cloud base is high, so that accretion of cloud water (>30%) is more important than the accretion of rain (<22%), and also greater in the High Plains than in the subtropics (Fig. 20b). Moreover, snow is the most abundant hydrometeor in the High Plains except for graupel/hail (e.g., Fig. 8). The higher updraft and hail cores in the High Plains make accretion of snow (qhacs) more important there than in the subtropics (Fig. 20c). The warmer midlevels in the subtropics enable more supercooled rain to survive and collide with snow and cloud ice before autoconversion occurs, so that hail production by snow and cloud ice accreting rain are significant in the subtropics (Fig. 20d,e).

The sinks of hail are plotted in Fig. 21. As discussed previously in regard to the production of rain, the maximum hail concentration in the subtropical storms is farther from the updraft core, and in weaker ascent, than in the High Plains cases. For the same reasons as stated in the context of rain production earlier in this chapter, most hail depletion in the subtropics comes from shedding (Fig. 21a) instead of melting (Fig. 21b). Also, for reasons stated therein, the falling hail/graupel in the High Plains storms undergoes more melting (Fig. 21b) than shedding (Fig. 21a). Because the environment in the subtropics is moister than in the High Plains, as shown in the soundings, sublimation (qssbv) is smaller in the subtropics than in the High Plains (Fig. 21c).

## 7. Conclusions

In this study we have examined the microphysical features of warm-season maritime subtropical versus High Plains convective storms by using a three-dimensional nonhydrostatic numerical model to investigate the various microphysical processes that produce and deplete precipitation in the convective systems. This study has identified which physical processes play a primary role in the initiation and production of this precipitation. It also shows that microphysical structure and precipitation processes after the thunderstorms mature and stabilize are climate-dependent.

The ratio of ice mass to liquid mass in the maritime subtropics is  $\sim 1:1$ , versus  $\sim 7:3$  in the northern High Plains. We have also seen that the same hydrometeor types in the different climates have their favored microphysical processes for growth and decay. These findings not only demonstrate that thunderstorm structure depends on local dynamic and thermodynamic atmospheric conditions that are generally climate-dependent, but also provide information about the partitioning of hydrometeors in the thunderstorms.

Reliable microphysical datasets are needed to evaluate detailed cloud models, to guide the development of parameterizations for climate models, and to validate microphysical products obtained from passive satellite measurements. Because of the latent heat energy exchange by phase transformations and the different radiative characteristics of contrasting phases, the interrelationship between microphysical and radiative cloud properties calls for prime emphasis upon the understanding and modeling of climate processes. Better understanding of their workings can illuminate the mechanisms that influence the storms' precipitation efficiency in general, as well as the feedback between precipitation formation and storm dynamics.

Moreover, recent studies show that global circulation models (GCMs) are highly sensitive to the simulated water substance fields (e.g., Fowler et al., 1996; Fowler and Randall, 1996a,b). Thunderstorms occur daily and nearly everywhere on the earth. Hence, without knowledge of the global partitioning of hydrometeors in the storms, any calculations from model assumptions will be questionable. The current study and results therefrom can be applied toward filling this lack, but further studies for a wider range of climatic/geographical regimes will provide detailed information about the global partitioning of hydrometeors in the storms.

The prestorm environments shown in Fig. 1 suggest the differences between maritime subtropical and northern High Plains regions. The initial conditions from the soundings provide thermodynamical and dynamical information, which can then be highly related to the partitioning of hydrometeors and dominant microphysical processes in the different regions. An in-depth investigation is needed to find the relationships. The future findings, and any resulting advances in convective parameterization, will potentially benefit the forecasting and modeling communities.

## Acknowledgments

This material is based upon work partially supported by the National Science Foundation under Grants Nos. ATM-0234744 and ATM-0244505, and by the National

Aeronautic and Space Administration under Grant No. NAG5-7605. Any opinions, findings, conclusions or recommendations expressed in this material are those of the authors and do not necessarily reflect the views of the National Science Foundation and the National Aeronautic and Space Administration.

## References

- Arakawa, A., Schubert, W.H., 1974. Interaction of a cumulus cloud ensemble with the large-scale environment, Part I. *J. Atmos. Sci.* 31, 674–701.
- Clark, T.L., 1977. A small scale dynamic model using a terrain-following coordinate transformation. *J. Comput. Phys.* 24, 186–215.
- Cotton, W.R., Stephens, M.A., Neuhorn, T., Tripoli, G.J., 1982. The Colorado State University three-dimensional cloud/mesoscale model—1982: Part II. An ice phase parameterization. *J. Rech. Atmos.* 16, 295–320.
- Cotton, W.R., Tripoli, G.J., Rauber, R.M., Mulvihill, E.A., 1986. Numerical simulation of the effects of varying ice crystal nucleation rates and aggregation processes on orographic snowfall. *J. Clim. Appl. Meteorol.* 25, 1658–1680.
- Emanuel, K.A., Živković-Rothman, M., 1999. Development and evaluation of a convection scheme for use in climate models. *J. Atmos. Sci.* 56, 1766–1782.
- Fankhauser, J.C., 1982. The June 22, 1976 case study: large scale influences, radar structure, and mesoscale circulation. In: Knight, C.A., Squires, P. (Eds.), *Hailstorm of the Central High Plain, Vol. II: Case Studies of the National Hail Research Experiment*. Colorado Associated Universities Press, Boulder, CO, pp. 1–34.
- Flossmann, Andrea I., 1998. Interaction of aerosol particles and clouds. *J. Atmos. Sci.* 55, 879–887.
- Flossmann, A.I., Pruppacher, H.R., 1988. A theoretical study of the wet removal of atmospheric pollutants: Part III. The uptake, redistribution, and deposition of  $(\text{NH}_4)_2\text{SO}_4$  particles by a convective cloud using a two-dimensional cloud dynamics model. *J. Atmos. Sci.* 45, 1857–1871.
- Flossmann, A.I., Hall, W.D., Pruppacher, H.R., 1985. A theoretical study of the wet removal of atmospheric pollutants: Part I. The redistribution of aerosol particles captured through nucleation and impaction scavenging by growing cloud drops. *J. Atmos. Sci.* 42, 583–606.
- Flossmann, A.I., Pruppacher, H.R., Topalian, J.H., 1987. A theoretical study of the wet removal of atmospheric pollutants: Part II. The uptake and redistribution of  $(\text{NH}_4)_2\text{SO}_4$  particles and  $\text{SO}_2$  gas simultaneously scavenged by growing cloud drops. *J. Atmos. Sci.* 44, 2812–2923.
- Foote, G.B., 1984. A study of hail growth utilizing observed condition. *J. Clim. Appl. Meteorol.* 23, 84–101.
- Fowler, L.D., Randall, D.A., 1996a. Liquid and ice cloud microphysics in the CSU general circulation model: Part III. Sensitivity to modeling assumptions. *J. Climate* 9, 561–586.
- Fowler, L.D., Randall, D.A., 1996b. Liquid and ice cloud microphysics in the CSU general circulation model: Part II. Impact on cloudiness, the earth's radiation budget, and the general circulation of the atmosphere. *J. Climate* 9, 530–560.
- Fowler, L.D., Randall, D.A., Rutledge, S.A., 1996. Liquid and ice cloud microphysics in the CSU general circulation model: Part I. Model description and simulated microphysical processes. *J. Climate* 9, 489–529.
- Frei, C., Schär, C., Lüthi, D., Davies, H.C., 1998. Heavy precipitation processes in a warmer climate. *Geophys. Res. Lett.* 25, 1431–1434.
- Grabowski, W.W., 2000. Cloud microphysics and the tropical climate: cloud-resolving model perspective. *J. Climate* 13, 2306–2322.
- Gregory, J.M., Mitchell, J.F.B., 1995. Simulation of daily variability of surface temperature and precipitation over Europe in the current and  $2 \times \text{CO}_2$  climate using the UKMO high-resolution climate model. *Q. J. Royal Meteorol. Soc.* 121, 1451–1476.
- Colquhoun, D.J., Batt, J.R., Casinadar, K.L., 1993. Severe thunderstorms in New South Wales. *Clim. Change* 25, 369–388.
- Johnson, D.E., Wang, P.K., Straka, J.M., 1993. Numerical simulations of the 2 August 1981 CCOPE supercell storm with and without ice microphysics. *J. Appl. Meteorol.* 32, 745–759.
- Johnson, D.E., Wang, P.K., Straka, J.M., 1994. A study of microphysical process in the August 1981 CCOPE supercell storm. *Atmos. Res.* 33, 93–123.

- Jou, J.D., 1994. Mountain-originated mesoscale precipitation system in northern Taiwan: a case study 21 June 1991. *Terr. Atmos. Ocean. Sci.* 5, 169–197.
- Keeling, C.D., Whorf, T.P., 2003. Atmospheric CO<sub>2</sub> records from sites in the SIO air sampling network. In *Trends: A Compendium of Data on Global Change*. Carbon Dioxide Information Analysis Center, Oak Ridge National Laboratory, U.S. Department of Energy, Oak Ridge, TN, U.S.A.
- Kessler, E., White, G.F., 1981. Thunderstorms in a social context. In: Kessler, E. (Ed.), *Thunderstorms: A Social, Scientific and Technological Documentary*, vol. 1. U.S. Department of Commerce, Washington, DC, pp. 1–22.
- Klemp, J.B., Wilhelmson, R.B., 1978. The simulation of three-dimensional convective storm dynamics. *J. Atmos. Sci.* 35, 1070–1096.
- Klimowski, B.A., 1994. Initiation and development of rear inflow within the 28–29 June 1989 North Dakota mesoconvective system. *Mon. Weather Rev.* 122, 765–779.
- Kubesh, R.J., Musil, D.J., Farley, R.D., Orville, H.D., 1988. The 1 August 1981 CCOPE storm: observations and modeling results. *J. Appl. Meteorol.* 27, 216–243.
- Kuo, H.L., 1974. Further studies of the parameterization of the influence of cumulus convection on large-scale flow. *J. Atmos. Sci.* 31, 1232–1240.
- Lin, H.-M., 2000. The microphysical characteristics of summer time thunderstorms in subtropics and High Plains from a 3-D model simulation. PhD thesis, Univ. of Wisconsin-Madison, U.S.A., 295 pp.
- Lin, H.-M., Wang, P.K., 1997. A numerical study of microphysical processes in the 21 June 1991 northern Taiwan mesoscale precipitation system. *Terr. Atmos. Ocean. Sci.* 8, 385–404.
- Lin, Y.L., Farley, R.D., Orville, H.D., 1983. Bulk parameterization of the snow field in a cloud model. *J. Clim. Appl. Meteorol.* 22, 1065–1092.
- Manabe, S., Smagorinsky, J., Strickler, R., 1965. Simulated climatology of a general circulation model with a hydrologic cycle. *Mon. Weather Rev.* 93, 769–798.
- Michaels, P.J., Stooksbury, D.E., 1992. Global warming: a reduced threat? *Bull. Am. Meteorol. Soc.* 73, 1563–1577.
- Miller, L.J., Tuttle, J.D., Knight, C.A., 1988. Airflow and hail growth in a severe northern High Plain supercell. *J. Atmos. Sci.* 45, 736–762.
- Musil, D.J., Heymsfield, A.J., Smith, P.L., 1986. Microphysical characteristics of a well-developed weak echo region in a High Plains supercell thunderstorm. *J. Clim. Appl. Meteorol.* 25, 1037–1051.
- Orville, H.D., Kopp, F.J., Nair, U.S., Stith, J.L., Rinehart, R.E., 1990. On the origin of ice in strong convective cells. *Conf. Cloud Physics, San Francisco, CA. Am. Meteorol. Soc., Boston, MA*, pp. 16–20.
- Priest, C., Rind, D., 1994. The impact of a 2 × CO<sub>2</sub> climate on lightning-caused fires. *J. Climate* 7, 1484–1494.
- Ramachandran, P., Detwiler, A., Helsdon Jr., J., Smith, P.L., Bringi, V.N., 1996. Precipitation development and electrification in Florida thunderstorm cells during convection and precipitation/electrification project. *J. Geophys. Res.* 101, 1599–1619.
- Straka, J.M., 1989. Hail growth in a highly glaciated central High Plains multi-cellular hailstorm. PhD thesis, Univ. of Wisconsin-Madison, U.S.A., 413 pp.
- Tremback, C.J., Powell, J., Cotton, W.R., Pielke, R.A., 1987. The forward-in-time upstream advection scheme: extension to higher orders. *Mon. Weather Rev.* 115, 540–555.
- Wade, C.G., 1982. A preliminary study of an intense thunderstorm which moved across the CCOPE research network in southeastern Montana. *Proc. Ninth Conf. On Weather Forecasting and Analysis, Seattle, WA. Am. Meteorol. Soc., Boston, MA*, pp. 388–395.
- Wang, P.K., 2003. Moisture plumes above thunderstorm anvils and their contributions to cross tropopause transport of water vapor in midlatitudes. *J. Geophys. Res.* 108 (D6), 4194.
- Wang, P.K., 2004. A cloud model interpretation of jumping cirrus above storm top. *Geophys. Res. Lett.* 31, L18106.
- Yuter, S.E., Houze Jr., R.A., 1995a. Three-dimensional kinematic and microphysical evolution of Florida cumulonimbus. Part I: spatial distribution of updrafts, downdrafts and precipitation. *Mon. Weather Rev.* 123, 1921–1940.
- Yuter, S.E., Houze Jr., R.A., 1995b. Three-dimensional kinematic and microphysical evolution of Florida cumulonimbus: Part II. Frequency distributions of vertical velocity, reflectivity, and differential reflectivity. *Mon. Weather Rev.* 123, 1941–1963.